

Article

Not peer-reviewed version

---

# Hypergraph Analysis of Functional Brain Connectivity During Figurative Attention

---

[Alexander N. Pisarchik](#)<sup>\*</sup>, Natalia Peña Serrano, [Walter Escalante Puente de la Vega](#), [Rider Jaimes-Reátegui](#)

Posted Date: 25 February 2025

doi: 10.20944/preprints202502.1998.v1

Keywords: hypergraph; brain connectivity; cognitive neuroscience; visual perception; electroencephalography (EEG); coherence; cross-correlation; mutual information; neuronal networks




Preprints.org is a free multidisciplinary platform providing preprint service that is dedicated to making early versions of research outputs permanently available and citable. Preprints posted at Preprints.org appear in Web of Science, Crossref, Google Scholar, Scilit, Europe PMC.

Copyright: This open access article is published under a Creative Commons CC BY 4.0 license, which permit the free download, distribution, and reuse, provided that the author and preprint are cited in any reuse.

## Article

# Hypergraph Analysis of Functional Brain Connectivity During Figurative Attention

Alexander N. Pisarchik <sup>1\*</sup>, Natalia Peña Serrano <sup>2</sup>, Walter Escalante Puente de la Vega <sup>1</sup> and Rider Jaimes-Reátegui <sup>3</sup>

<sup>1</sup> Centro de Tecnología Biomédica, Universidad Politécnica de Madrid, Campus de Montegancedo, Pozuelo de Alarcón, 28223 Madrid, Spain

<sup>2</sup> Instituto de Fisiología Celular, Universidad Nacional Autónoma de México, Coyoacán, 04510 Ciudad de México, México

<sup>3</sup> Departamento de Ciencias Exactas y Tecnología, Centro Universitario de los Lagos, Universidad de Guadalajara, Enrique Díaz de León 1144, Colonia Paseos de la Montaña, Lagos de Moreno, Jalisco, Mexico

\* Correspondence: alexander.pisarchik@ctb.upm.es

**Abstract:** Hypergraph analysis extends traditional graph theory by enabling the study of complex, many-to-many relationships in networks, offering powerful tools for understanding brain connectivity. This case study introduces a novel methodology for constructing both graphs and hypergraphs of functional brain connectivity during figurative attention tasks, where subjects interpret the ambiguous Necker cube illusion. Using a frequency-tagging approach, we simultaneously modulated two cube faces at distinct frequencies while recording electroencephalography (EEG) responses. Brain connectivity networks were constructed using multiple measures - coherence, cross-correlation, and mutual information - providing complementary insights into functional relationships between regions. Our hypergraph analysis revealed distinct connectivity patterns associated with attending to different cube orientations, including previously unobserved higher-order relationships between brain regions. The results demonstrate bilateral cortico-cortical interactions and suggest integrated processing hubs that may coordinate visual attention networks. This methodological framework not only advances our understanding of the neural basis of visual attention but also offers potential applications in attention monitoring and clinical assessment of attention disorders. While based on a single subject, this proof-of-concept study establishes a foundation for larger-scale investigations of brain network dynamics during ambiguous visual processing.

**Keywords:** hypergraph, brain connectivity, cognitive neuroscience, visual perception, electroencephalography (EEG), coherence, cross-correlation, mutual information, neuronal networks.

## 1. Introduction

Understanding brain connectivity in response to external stimuli is essential for uncovering the mechanisms behind information processing, perception, attention, and decision-making. Functional connectivity, which identifies active brain regions exhibiting correlated frequency, phase, and amplitude, can be analyzed in both frequency and time domains [1]. When a sufficiently large population of neurons synchronizes, their collective electrical activity becomes detectable through brain imaging techniques such as electroencephalography (EEG). To examine the emergence and dynamic evolution of functional brain networks, researchers often apply complex network theory, grounded in mathematical graph theory [2,3]. By representing brain regions as nodes and their interactions as links, this approach has facilitated the study of biorhythmic connections across different brain areas [4,5]. It has also proven valuable in identifying individual cognitive differences [6], diagnosing neurological disorders [7–9], and assessing aging-related neural changes [10–13].

EEG-based functional connectivity networks have become essential tools for understanding individual variability in brain activation patterns during cognitive tasks [14,15]. These networks provide valuable insights into how different brain regions interact, shedding light on the neural mechanisms

underlying attention and other cognitive processes. Traditional graph-theoretic approaches model functional connectivity by representing brain regions as vertices and their functional interactions as edges [4]. However, these methods primarily capture second-order relationships—interactions between pairs of brain regions—while neglecting higher-order relationships that are fundamental to complex neural processing.

Since cognitive processes such as attention involve dynamic and multifaceted interactions across multiple brain regions, conventional functional connectivity networks fail to provide a complete picture by only capturing pairwise relationships. To overcome this limitation, hypergraph-based connectivity models have been introduced. Unlike traditional graphs, hypergraphs allow for the representation of multi-node interactions through hyperedges, enabling a richer and more comprehensive characterization of brain connectivity.

Hypergraphs have recently gained prominence as an advanced framework for investigating brain connectivity [16–30]. Unlike conventional graphs that are limited to pairwise relationships, hypergraphs extend graph theory to model complex, multi-region interactions simultaneously [31,32]. This approach offers a more nuanced and holistic view of functional brain networks by capturing the intricate, dynamic interactions among multiple neural regions. Through hypergraph analysis, researchers can gain deeper insights into how brain regions integrate, synchronize, and adapt to support cognitive functions, providing novel perspectives on neural organization and functionality.

Hypergraphs representing brain connectivity have been constructed using neurophysiological data from various imaging modalities. Most studies have focused on functional magnetic resonance imaging (fMRI) data, particularly in the resting state [16–20,22–24,33]. Structural MRI has also been employed for hypergraph-based connectivity modeling [25]. Additionally, researchers have developed hypergraphs using multimodal data that integrate MRI with fluorodeoxyglucose positron emission tomography (PET) and cerebrospinal fluid analysis [29]. Beyond MRI-based studies, both invasive intracranial EEG [26] and noninvasive EEG [27,28] have been used to construct hypergraphs. Magnetoencephalography (MEG) data have also been explored in hypergraph-based connectivity studies [30].

The versatility of hypergraph-based connectivity modeling has led to applications in diverse areas, including emotion recognition [22,27], motor imagery [28], and the diagnosis of neurological disorders such as mild cognitive impairment [18,29,33], schizophrenia [20], autism spectrum disorder (ASD) [24], Alzheimer's disease [25,29], and epileptic seizure detection [26]. Many of these studies employ correlation-based metrics to measure functional connectivity, with Pearson correlation being a widely used approach for quantifying neural interactions [34]. Given the importance of attentional processes in cognitive health, hypergraph-based connectivity models offer a promising avenue for understanding the neural mechanisms underlying attention and related cognitive functions.

Attention is a crucial cognitive function, and its impairment is associated with various neurological and psychiatric disorders, including cognitive decline, dementia, attention deficit hyperactivity disorder (ADHD), and autism spectrum disorder (ASD). These conditions affect a broad range of cognitive and behavioral abilities, such as learning, problem-solving, communication, and social interaction. Individuals with attention deficits may struggle to express their experiences or understand others' perspectives, which can hinder their development of essential social and learning skills. Electroencephalography (EEG) is a widely used modality for assessing attention. While many studies have focused on the relationship between P-300 event-related potentials and attention in EEG signals, others have explored spectral analysis as an alternative approach [35–39]. The use of hypergraphs to model brain connectivity could provide deeper insights into the neural mechanisms underlying attention deficits, particularly in disorders like ASD and ADHD, by capturing the complex, multi-dimensional relationships within brain networks. This approach may complement traditional EEG-based methods, offering a more comprehensive understanding of attention-related impairments and their neural correlates.

This study is motivated by the growing interest in machine learning techniques for the early diagnosis and prediction of neurodegenerative diseases based on hypergraphs of brain connectivity. Our aim is to demonstrate how hypergraphs can be constructed to represent brain connectivity patterns associated with attention, which may, in the future, contribute to the diagnosis and prediction of attention-related disorders. To the best of our knowledge, this work presents the first hypergraph-based analysis of functional brain connectivity associated with attention. Using EEG data from a subject exhibiting strong attentional engagement, we construct both pairwise graphs and hypergraphs based on three important connectivity measures—coherence [40], cross-correlation [41], and mutual information [42]. Our analysis investigates how functional connectivity differs when the subject actively focuses on one interpretation of the Necker cube's orientation compared to a neutral attentional state.

The remainder of this paper is organized as follows: Section 2 introduces the mathematical foundations underlying our methods. Section 3 details the experimental paradigm and methodology. Section 4 describes the procedures for analyzing the experimental EEG data. Sections 5 and 6 present results on the construction of attention-based pairwise graphs and hypergraphs, respectively. Section 7 provides an in-depth discussion of our findings, followed by key conclusions in Section 8. Additional details on graph construction are included in Appendices.

## 2. Mathematical Basis

In this section, we provide with the most important definitions of pairwise graphs and hypergraphs, as well as the measures of brain connectivity which we utilize in this study: coherence, cross-correlation, and mutual information.

### 2.1. Main Definitions

A *plain graph*  $G$  is an abstract mathematical structure composed of a finite set of  $n$  vertices (or nodes)  $V$  and a set of  $m$  edges (or links)  $E$ , where each edge represents an interaction between a pair of vertices. Mathematically, the plain graph is defined as

$$G = (V, E), \quad V = \{v_1, \dots, v_i, \dots, v_n\}, \quad E = \{v_1, \dots, v_j, \dots, v_m\}. \quad (1)$$

The plain graph is commonly represented by its adjacency matrix  $A$ , which can be either binary (indicating the presence or absence of a connection between two vertices) or numerical (reflecting the strengths or weights of the connections between edges). A graph with labels assigned to its edges and vertices is referred to as a *labeled graph*. A label of edge  $j$  is its weight  $w(e_j)$  (or connectivity measure), i.e.,  $\text{Lab}(e_j) = w(e_j)$ , while a label of vertex  $i$  is the sum of weights of all edges which connect this vertex with other nodes, i.e.,

$$\text{Lab}(v_i) = \sum_j^m w(e_j)_{\{e_j \sim v_i\}}, \quad (2)$$

where  $w(e_j)_{\{e_j \sim v_i\}}$  is the indicator function, equal to weight  $w(e_j)$  of edge  $j$  if this edge is incident to vertex  $i$ , and 0 otherwise.

In contrast to a plain graph, where an edge connects only two vertices, a *hypergraph* generalizes this concept by allowing a single edge, called a *hyperedge*, to connect more than two vertices [31, 32]. Formally, a hyperedge is defined as a collection of links that connect two or more edges with significantly correlated temporal or spectral profiles. Thus, a hypergraph is defined by a set of such hyperedges and nodes, offering a powerful framework for modeling and analyzing complex relationships, particularly in systems such as brain networks.

To illustrate this, consider a brain neural network that is conventionally partitioned into  $n$  distinct regions, referred to as nodes or vertices. Signals from these regions can be recorded using various neuroimaging modalities, such as EEG, MEG, or fMRI. When the brain is exposed to a stimulus, neuronal activity in specific regions associated with the stimulus is either activated or deactivated, and



information about this process is encoded in the corresponding vertices. By capturing the relationships between these regions, a hypergraph  $\mathbf{H}$  is defined by a set of  $n$  vertices  $\mathbb{V}$  and a set of  $m$  hyperedges  $\mathbb{E}$  as

$$\mathbf{H} = (\mathbb{V}, \mathbb{E}), \quad \mathbb{V} = \{v_1, v_2, \dots, v_i, \dots, v_n\}, \quad \mathbb{E} = \{e_1, e_2, \dots, e_j, \dots, e_m\}, \quad (3)$$

where each hyperedge  $e_j \in \mathbb{E}$  represents a specific measure of connectivity. In this work, we consider widely used measures of brain connectivity, such as coherence, cross-correlation, and mutual information. These measures can be computed for specific spectral bands and time intervals of interest, allowing for a detailed characterization of functional relationships within the brain.

A hypergraph is characterized by its *order* and *size*. The order refers to the number of vertices  $|\mathbb{V}| = n$ , while the size corresponds to the number of hyperedges  $|\mathbb{E}| = m$ . Furthermore, both vertices and hyperedges are associated with a degree (Deg), which quantifies their connectivity within the hypergraph. Specifically, the degree of a vertex  $v \in \mathbb{V}$  is defined as the number of hyperedges incident to it, whereas the degree of a hyperedge  $e \in \mathbb{E}$  is defined as the number of vertices incident to it. Mathematically, these degrees can be expressed as:

$$\text{Deg}(v) = \sum_{e \in \mathbb{E}} 1_{\{v \in e\}} \quad \text{and} \quad \text{Deg}(e) = \sum_{v \in \mathbb{V}} 1_{\{v \in e\}}, \quad (4)$$

where  $1_{\{\cdot\}}$  is the indicator function, equal to 1 if the condition is satisfied and 0 otherwise. These degree measures provide insights into the topological structure of the hypergraph, highlighting the centrality of vertices and the complexity of hyperedges in capturing higher-order interactions.

If a vertex  $v$  is covered by two or more hyperedges, we say that these hyperedges are adjacent through  $v$  ( $e_i \sim v_j$ ). Similarly, the vertices covered by a hyperedge  $e$  are considered adjacent through  $e$  ( $v_j \sim e_i$ ).

A hypergraph  $\mathbf{H}$  can be represented in several equivalent forms, including an incidence graph, an incidence matrix  $\mathbf{H} = \{0, 1\}^{|\mathbb{V}| \times |\mathbb{E}|}$ , and a hyperedge weight matrix  $\mathbf{W}$ .

An *incidence graph* (also known as a bipartite graph representation) is a way to represent a hypergraph by transforming it into a standard graph. In this representation, the hypergraph's vertices and hyperedges are treated as two distinct sets of nodes in a bipartite graph.

The *incidence matrix* is defined as

$$\mathbf{H}[i][j] = \begin{cases} 1, & \text{if } v_i \in e_j, \\ 0, & \text{otherwise,} \end{cases} \quad (5)$$

where  $v_i \in \mathbb{V}$  represents the  $i$ -th vertex and  $e_j \in \mathbb{E}$  represents the  $j$ -th hyperedge. This matrix captures the membership of vertices in hyperedges, providing a binary representation of the hypergraph structure.

A *hyperedge weight matrix*  $\mathbf{W}$  encodes the significance of each hyperedge in the hypergraph. Specifically, the weight of each hyperedge  $e_j$  is located at the corresponding diagonal entry of  $\mathbf{W}$ , such that:

$$\text{diag}(\mathbf{W}) = [w(e_1), w(e_2), \dots, w(e_{|\mathbb{E}|})], \quad (6)$$

where  $w(e_j)$  represents the weight of the  $j$ -th hyperedge. In this work, the weight  $w(e_j)$  is defined as the degree of the hyperedge  $e_j$ , i.e.,  $\text{Deg}(e_j)$ . This weighting scheme reflects the topological importance of each hyperedge within the hypergraph.

## 2.2. Summarization

Graphs of real datasets are often very massive. For example, the graph constructed on the base of the MEG data has 306 nodes, each representing time series recorded by magnetic sensors [30,43]. The manipulation with such large networks requires high computational capacity and extensive time. To decrease the communicational cost, a graph summarization technique is used [44]. Summarization methods allow one to reduce the graph size by extracting the most important information from the

original graph. Then, the resultant summary graph can be queried, analyzed, and understood more efficiently using existing tools and algorithms. The resultant graph can easier visualize the dataset that is originally too large to load into memory. In addition, real graph data are frequently large scale and considerably noisy with many hidden, unobserved, or erroneous links and labels. Such noise hinders analysis by increasing the workload of data processing and hiding the more important information. Summarization serves to filter out noise and reveal specific features in the data.

Summarization is application dependent and can be made using various methods. The most popular summarization techniques are node grouping and edge grouping. While the node-grouping methods recursively aggregate nodes into “supernodes” based on an application-dependent optimization function, which can be based on structure and/or attributes, e.g., clustering techniques and map each densely connected cluster to a supernode, edge-grouping methods aggregate edges into hyperedges. In this paper, we apply the latter approach that compresses neighborhoods around high-degree nodes, accelerating query processing and enabling direct operations on the compressed graph. The edge-grouping method was used by Maccioni and Abadi [45], who introduced “compressor nodes,” which represent common connections high-degree nodes. They assumed that high-degree nodes are surrounded by redundant information that can be synthesized and eliminated. To provide global guarantees and reduce the scope of compressor handling during query processing, dedensification only occurs when every node has at most one outgoing edge to a compressor node, and every high-degree node has incoming edges coming only from a compressor node. These guarantees are then used to create query processing algorithms that enable direct pattern matching queries on the compressed graph.

Other summarization techniques imply simplification or sparsification. These methods streamline an input graph by removing less “important” nodes or edges, resulting in a sparsified graph. In the brain connectivity network, some edges are more indicative of predicting cognitive performance. Therefore, the node grouping layer is designed to “hide” the non-indicative (‘noisy’) edges by grouping them into a cluster (supernode), thus highlighting the indicative edges. Finally, there are influence-based approaches which aim to discover a high-level description of the influence propagation in large-scale graphs. Techniques in this category formulate the summarization problem as an optimization process in which some quantity related to information influence is maintained.

The output of a summarization procedure can take one of two forms: (i) a sparsified graph, which retains only a subset of nodes and/or edges from the original graph, or (ii) a hypergraph composed of selected nodes united by hyperedges. Unlike traditional graphs, hypergraphs allow nodes to belong to multiple hyperedges, enabling the representation of complex, higher-order relationships within the data. In this paper, we integrate both approaches, leveraging sparsified graphs as a foundation to construct hypergraphs that model brain connectivity associated with attention. This combined methodology enables the capture of intricate neural interactions while maintaining computational efficiency, providing a robust framework for analyzing attention-related brain networks.

### 2.3. Coherence

One of the key measures to quantify neuronal synchrony is event-related coherence [40,46,47]. It examines the frequency-domain relationship between two signals, reflecting the extent to which their spectral components are synchronized. Specifically, it assesses the consistency of the relative amplitude and phase between two signals within a given frequency range. Mathematically, it is a linear method that generates a symmetrical matrix, which lacks directional information. When two signals are identical, the coherence value is 1, whereas it approaches 0 as the signals become increasingly dissimilar. Since its introduction, coherence has been widely employed in brain connectivity studies involving both patients and healthy individuals. These studies span a diverse range of applications, including working memory [48], brain lesions [49], hemiparesis [50], resting-state networks [51], schizophrenia [52,53], responses to panic medications [54], and motor imagery [55]. Due to the inherent variability in human brains, distinct patterns of coherent neuronal activity have been observed across individuals. For instance, when exposed to flickering visual stimuli, subjects exhibit coherent responses in the

visual cortex at the flicker frequency and its harmonics, with varying sizes of coherent neural networks [43,56].

Coherence between two signals ( $X(t)$  and  $Y(t)$ ) is defined as

$$Coh_{XY}(f) = \frac{P_{XY}(f)^2}{P_{XX}(f)P_{YY}(f)}, \quad (7)$$

where  $P_{XX}(f)$  and  $P_{YY}(f)$  are the auto spectral densities of  $X(t)$  and  $Y(t)$  signals, respectively, and  $P_{XY}(f)$  is the cross-spectral density. The coherence function estimates the extent to which  $Y(t)$  may be predicted from  $X(t)$  by an optimum linear least squares function.

Coherence values always satisfy  $Coh_{XY}(f) \in [0, 1]$ . In our study, since we focus on the changes in coherence induced by attention ( $\Delta Coh$ ), these differences can be either positive or negative, thus satisfying  $\Delta Coh \in [-1, 1]$ . In the subsequent analysis, we will refer to an increase in coherence ( $\Delta Coh > 0$ ) as *coherence* and a decrease in coherence ( $\Delta Coh < 0$ ) as *anticoherence*. This distinction allows us to better characterize the dynamic shifts in neural connectivity associated with attentional processes.

#### 2.4. Cross-Correlation

Unlike previous studies that rely on Pearson correlation for constructing functional connectivity networks [57,58], our approach employs cross-correlation analysis. Pearson correlation has several limitations, including sensitivity to delays in neural responses and potential confounding effects from other brain regions. To address these issues, we used cross-correlation analysis, selecting the optimal time delay at which correlation is maximized.

Cross-correlation measures the similarity between two time series as a function of the time lag between them. This method provides a robust and sensitive approach for analyzing EEG signals recorded simultaneously from different channels, independent of their amplitudes [41]. By accounting for time lags, cross-correlation allows for the evaluation of relationships between signals not only at the same moment but also at different time points, offering deeper insights into temporal dependencies and synchronization patterns in neural activity.

The normalized cross-correlation between two EEG channels  $x(t)$  and  $y(t)$ , at a given time lag  $\tau$ , is calculate as:

$$Corr_{xy}(\tau) = \frac{\sum_t (x(t) - \bar{x})(y(t + \tau) - \bar{y})}{\sqrt{\sum_t (x(t) - \bar{x})^2 \sum_t (y(t) - \bar{y})^2}}, \quad (8)$$

where  $\bar{x}$  and  $\bar{y}$  demote the mean values of  $x(t)$  and  $y(t)$ , respectively. For each pair of channels, we identify the time lag  $\tau$  at which  $Corr_{xy}$  attains its maximum value and use this peak correlation value in our subsequent analysis. This approach ensures that we capture the strongest temporal relationship between the signals, providing a robust basis for reconstructing functional connectivity network.

Cross-correlation values range from  $-1$  and  $1$ . To analyze changes in cross-correlation induced by attention, we define the difference in cross-correlation ( $\Delta Corr$ ), which can take values between  $-2$  and  $2$ . For clarity, we refer to cases where  $\Delta Corr > 0$  as *correlation* and cases where  $\Delta Corr < 0$  as *anticorrelation*. This distinction helps characterize neural connections that emergent (increased synchrony) and disappear (decreased synchrony) due to attention.

#### 2.5. Mutual Information

Since its introduction by Shannon [59] mutual information has been used across various fields to quantify coupling or information transmission between systems [60]. In neuroscience, several studies have employed mutual information analysis to investigate information transfer in the brain. For example, Jeong et al. [42] applied this method to multi-channel EEG data to assess information flow between cortical regions in Alzheimer's disease (AD) patients.

Cross mutual information (CMI) measures the information gained about one system from observing another, in contrast to auto mutual information, which quantifies mutual information between

two parts of the same time series  $x(t)$  separated by a lag  $\tau$ . Unlike traditional correlation functions, which capture only linear dependencies, CMI detects both linear and nonlinear statistical relationships between time series. CMI between measurement  $x_i$  from system  $X$  and  $y_j$  from system  $Y$  represents the amount of information  $x_i$  provides about  $y_j$ . Thus, CMI serves as a measure of dynamical coupling or information transmission between  $X$  and  $Y$ . When applied to EEG data, it can be interpreted as an indicator of functional connectivity between brain regions. If two systems are entirely independent, their CMI is zero, meaning no information is transmitted between them. Therefore, in our case, CMI quantifies the information flow between different brain areas.

CMI is calculated as

$$Inf(X, Y) = \sum_{x \in X} \sum_{y \in Y} p(x, y) \log_2 \left( \frac{p(x, y)}{p(x)p(y)} \right), \quad (9)$$

where  $p(x)$  and  $p(y)$  are the normalized histograms of the distributions of measurements  $x$  and  $y$ , respectively, and  $p(x, y)$  denotes their joint probability density.

In this study, we compute the time-delayed CMI,  $Inf(X(t), Y(t + \tau))$ , which quantifies mutual information between EEG signals from each pair of channels as a function of a time delay. To assess information transmission between different cortical areas, we select the peak CMI value within a time delay range of  $0 \pm 500$  ms for each electrode pair.

CMI measures the degree of dependence between  $X$  and  $Y$ , ranging from 0 and to entropy  $H$  of  $X$ . A value of  $Inf(X, Y) = 0$  indicates mutual independence, whereas  $Inf(X, Y) = H(X)$  signifies that one signal completely determines the other. Similar to coherence and correlation measures, changes in CMI due to attention ( $\Delta I$ ) can be either positive or negative. Specifically, positive values ( $\Delta I > 0$ ) indicate *information gain*, while negative values ( $\Delta I < 0$ ) correspond to *information loss*.

### 3. Materials and Methods

#### 3.1. Participant

In this case study, we analyze the EEG data of a healthy 22-year-old female subject, recorded during experiments using a flickering image paradigm. The study was conducted at the Center for Biomedical Technology, Universidad Politécnica de Madrid, Spain. This subject was selected from a pool of 28 subject participants as the one demonstrating the highest level of attention (subject #2 from [39]). Before the experiment began, the subject provided written informed consent, ensuring anonymized data processing and compliance with data protection regulations. The subject was also briefed on the experiment's objectives and duration. The EEG study followed the ethical guidelines of the Declaration of Helsinki and was approved by the Ethics Committee of the Universidad Politécnica de Madrid (Ethics Approval Code: 2020-096) prior to participant recruitment.

#### 3.2. Stimulus

The subject was presented with a visual stimulus – the Necker cube – displayed as a white line drawing on a black screen. The image, approximately  $10 \times 10$  cm in size, was shown on a 22-inch liquid crystal monitor with a refresh rate of 60 Hz and luminance of  $100 \text{ cd/m}^2$ . The Necker cube was chosen for its ambiguous nature, allowing for perceptual alternation between left and right orientations.

The cube's pixel brightness alternated between black (0 in an 8-bit format) and gray (200) following a square-wave modulation. This modulation was applied at frequencies  $f_L = 6.67$  Hz and  $f_R = 8.57$  Hz to the left and right faces of the cube, respectively, consistent with previous studies [43,56]. These modulation frequencies generated frequency tags in the fast Fourier transform (FFT) spectra of the EEG signal, particularly in spectral regions around  $6.15 < f_1 < 6.75$  and  $8.00 < f_2 < 8.60$  within the visual cortex. To present the visual stimuli, we developed custom software using the Psycopy and Python platforms.



### 3.3. Experimental Setup

The EEG signal was recorded using equipment from Brain Products GmbH, including an EEG amplifier, a standard wireless 16-channel cap, a reference channel, and a ground channel. The cap was fitted with slim wet electrodes from EASYCAP GmbH. To ensure optimal conductivity between the electrodes and the scalp, a conductive gel was applied to each electrode.

The experiments took place in a dimly lit room, with the subject seated comfortably in front of a computer monitor positioned 70 cm away. The visual stimulus subtended an approximately viewing angle of 8 degrees.

EEG data were sampled at a rate of 500 Hz. Brain signals were recorded using Brain Products Recorder software, which allowed real-time monitoring to ensure accurate signal accuracy and quality. Data acquisition was conducted using the proprietary software provided by Brain Products GmbH.

### 3.4. Experimental Paradigm

The experiment comprised a series of Necker cube presentations, each lasting approximately 30 seconds, with 20-second intervals between presentations. During these intervals, the subject was allowed to blink. EEG recordings were continuously conducted throughout cube observation to monitor brain activity in real time.

Before the main experiment, the participant underwent a training session using a non-flickering Necker cube to familiarize herself with distinguishing between left- and right-oriented perceptions. The subject was instructed to complete three tasks: (1) observing the first cube image without interpreting its orientation, (2) perceiving the second cube image as left-oriented, and (3) perceiving the third cube image as right-oriented.

In the main experiment, the subject performed similar tasks but with a flickering (modulated) Necker cube, as illustrated in Fig. 1. The first task involved passive observation of the cube without interpretation of its orientation (MI: modulated involuntary). In the second task (MLV: modulated left voluntary) and third task (MRV: modulated right voluntary), the subject was instructed to voluntarily perceive the cube as left- or right-oriented, respectively.

To minimize artifacts caused by eye movements and blinking, the subject was instructed to maintain focus on a red dot at the center of the cube and to avoid blinking during stimulus presentation. EEG preprocessing further reduced artifacts from involuntary eye movements and blinking.

Each task was repeated twice per participant, with a 2-minute break between trials to allow for rest. Before each experiment, electrode conductivity was assessed to ensure optimal signal quality, maintaining electrode impedance below 10 k $\Omega$ .

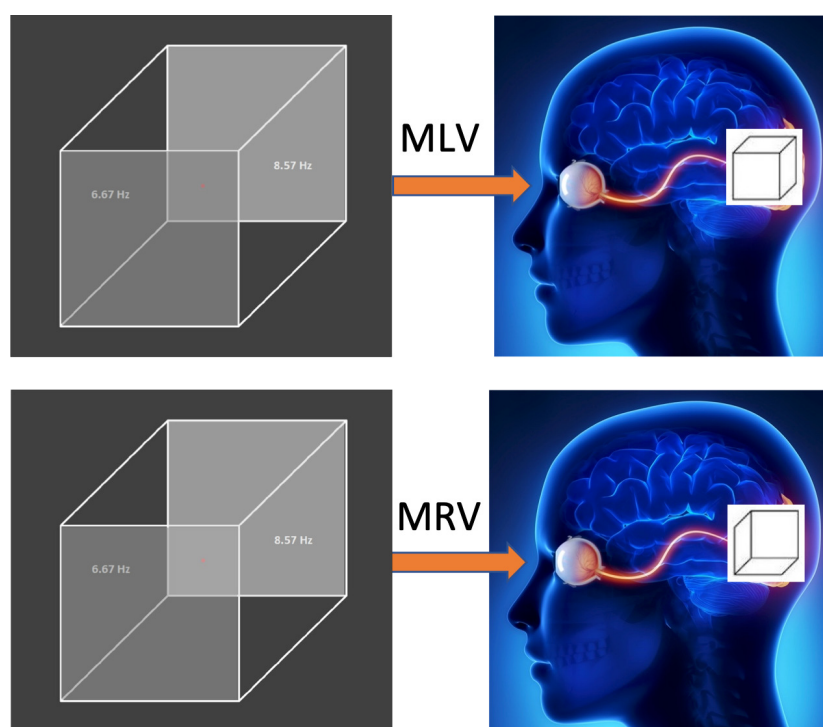


**Figure 1.** Visual stimulus. In the tasks MLV and MRV, the Necker cube with modulated left and right faces at frequencies 6.67 Hz and 8.57 Hz is voluntarily perceived as left- or right-oriented, respectively.

#### 4. Experimental Data Analysis

The preliminary analysis of the recorded EEG signals involved: (i) artifact removal to clean the raw data, (ii) frequency spectrum analysis to identify relevant frequency regions, and (iii) wavelet analysis to determine time intervals associated with voluntary attention.

The EEG data used in this study are available in the open dataset [61].

##### 4.1. Artifacts removal

The analysis of the raw EEG data started with artifact removal, one of the most critical aspects of data processing. To ensure optimal processing of EEG signals, we identified and eliminated endogenous artifacts (arising from within the subject) and exogenous artifacts (external to the subject), such as interference from nearby electronic equipment, flashing lights, environmental noise, facial muscle movements, and eye blinks.

First, we executed the following steps in data preprocessing: (1) After examining the raw signals, we identified time intervals that delineated the beginning and end of the response to applied visual stimulation. (2) We minimized a continuous global current trend throughout explored time intervals for each channel. This procedure improved the signal quality and facilitate the detection and correction of ocular artifacts during post-processing. (3) We removed endogenous and exogenous noise and focused on the frequencies of our stimuli. For these aims, we applied infinite impulse response (IIR) filters, specifically, 4th-order zero-phase shift Butterworth filters. Two types of filters were used: (i) band rejection (Notch Filter) to attenuate or eliminate the electrical network frequency (50 Hz in Spain) and the refresh rate of the monitor used for visual stimulation (120 Hz), with a bandwidth of 0.1 Hz, and (ii) 4th-order bandpass filter (BIF) of 4–20 Hz to concentrate on the frequencies of interest. These filters allowed us to filter out or attenuate unwanted frequency components present in the EEG signals.

Subsequently, we removed ocular artifacts, which can interfere with the detection and analysis of cortical responses, as electrical activity resulting from eye movements and blinking can contaminate brain signals. To ensure that these artifacts did not distort the results or complicate the analysis, we carefully examined the brain signals associated with visual stimuli. Since the eyes behave like a dipole, with the cornea serving as the positive part and the retina as the negative part of the dipole,

the identification of ocular artifacts is relatively straightforward. Vertical electro-oculogram artifacts (VEOG) and horizontal electro-oculogram artifacts (HEOG) exhibited electrical potentials ranging from 0.4 to 1.0 mV.

To mitigate the impact of ocular artifacts arising from vertical eye movements (VEOG) and lateral eye movements (HEOG) identified by inspection of raw time series, we employed the following methods:

- (i) Reference to frontal channels: Since our EEG equipment did not include electro-oculography electrodes, we used an electrode located in the frontal lobe (channel FP1) as VEOG, and channels F7 and F8 in the frontal lobe as left HEOG and right HEOG, respectively. Thus, the FP1 channel served as a common VEOG reference to detect vertical artifacts. Channels F7 and F8 acted as HEOG reference channels, similar to a bipolar electrode, to detect lateral artifacts occurring in the left and right hemispheres.
- (ii) Algorithm for reducing ocular artifacts: We employed semiautomated detection methods combined with independent component analysis (ICA). This approach enabled the effective identification and reduction of ocular artifacts in EEG signals, thus facilitating the subsequent analysis of cortical responses associated with the visual stimulus by eliminating or mitigating interference from eye movements and blinks.
- (iii) Value trigger algorithm: This algorithm facilitated the detection of characteristic patterns. Blinks were identified on the basis of their absolute magnitude, with definitive blink movements determined using the correlation method. The blink detection threshold (blink value trigger) was set at 97%, which means that any value above this threshold was recognized as a blink. The signal correlation was established at 70%. These values were experimentally determined by considering their influence on attenuating the signal of interest in the spectral regions of  $f_1$  and  $f_2$  in the occipital lobes (O1, Oz, O2 channels).

Lastly, we conducted ICA to find the optimal unmixing matrix to separate independent sources using statistical methods. To assess component independence, methods such as Maximum Negentropy, Kurtosis, Maximum Likelihood, and Mutual Information were employed. The optimization process for the optimal unmixing matrix ended when the maximum time independence of the components was achieved within a maximum number of steps or iterations. For this process, the extended nondeterministic INFOMAX algorithm with a maximum of 512 steps was selected as the optimal configuration. This ICA training method was adjusted after each convergence step to enhance signal separation. Convergence was deemed achieved when the algorithm reached a stable solution, favoring Independent Components (ICs) with Kurtosis ( $K$ ) values greater than 0 (indicating components with a non-Gaussian distribution) and less than 0 for noise, such as electrical network noise.

Following decomposition into ICs, quality control was performed by examining the number of steps used in decomposition of the ICs and comparing them with components initially flagged as possible ocular artifacts during visual inspection of the raw time series. As a final step, an inverse ICA of ICs and topographic retroprojection were performed to determine the brain lobes to which these possible signals corresponded. The analysis involved a comprehensive evaluation of the properties of IC, including their waveforms over time, energy, and kurtosis ( $K < 0$ ,  $K = 0$ ,  $K > 0$ ).

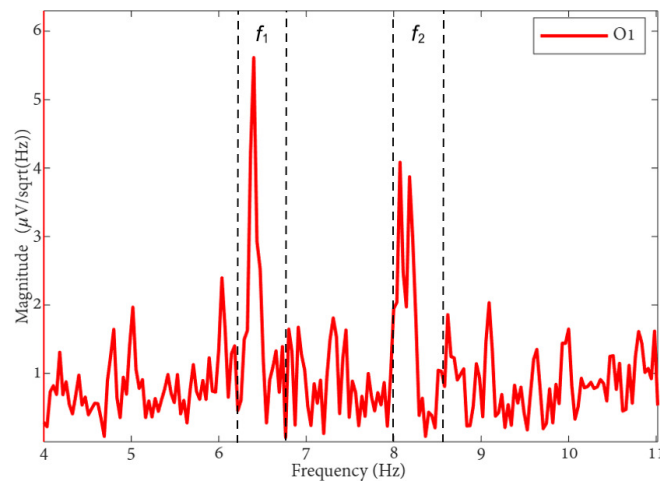
#### 4.2. Spectral Analysis

The FFT method enables the examination of a signal's frequency spectrum, which is essential for identifying frequency tags associated with flickering visual stimuli. In this study, we focus on the tag frequencies corresponding to the two perceived orientations of the Necker cube:  $f_L$  for the left-oriented cube and  $f_R$  for the right-oriented cube.

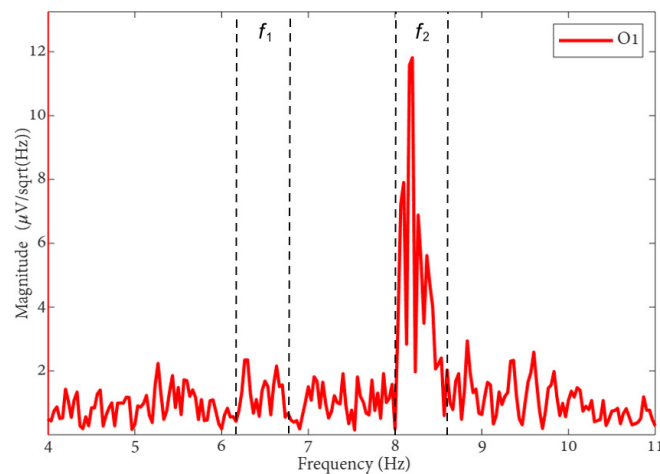
To ensure optimal analysis resolution, we implemented an FFT algorithm designed to operate on power-of-2 segmentations. This configuration maximized spectral resolution, allowing for efficient and precise signal decomposition in the frequency domain. As a result, we could efficiently identify the spectral characteristics associated with each cube orientation when analyzing EEG signals.

The FFT spectra of the MI, MLV, and MRV tests are shown in Figure 2. Distinct spectral peaks can be observed near the modulation frequencies within the ranges  $6.15 < f_1 < 6.75$  and  $8.00 < f_2 < 8.60$ . The brain does not respond on discrete frequencies due to two factors: (i) the modulation signal is not harmonic, and (ii) slight variation in the modulation signal occur throughout the experiment, influencing by computer load and memory fluctuations.

(a)



(b)



(c)

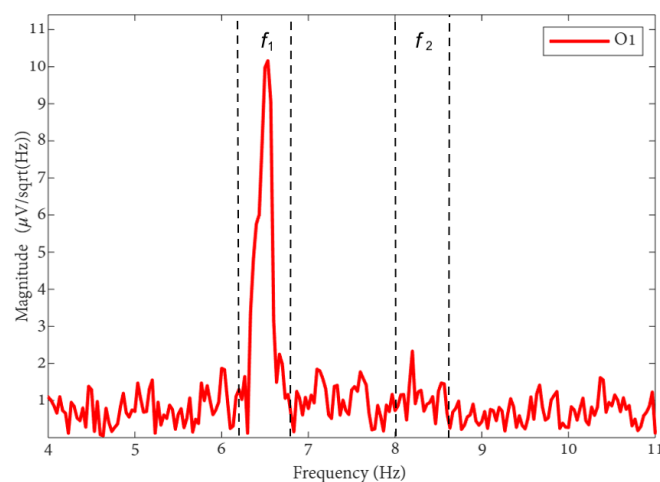


**Figure 2.** FFT spectra of preprocessed EEG from the O1 channel during (a) MI, (b) MRV, and (c) MLV tasks. The vertical dashed lines bound frequency regions of interest ( $f_1$  and  $f_2$ ), representing the brain response to stimulus modulation.



By comparing the spectrum obtained for involuntary attention (MI) shown in Figure 2(a) with the spectra for voluntary attention to the left-oriented cube (MLV) shown in Figure 2(b) and to the right-oriented cube (MRV) shown in Figure 2(c), it can be observed that the spectral amplitude at  $f_1$  dominates the amplitude at  $f_2$  when the subject perceives the cube as left-oriented (Figure 2(b)), and the spectral amplitude at  $f_2$  dominates the amplitude at  $f_1$  when the subject perceives the cube as right-oriented.

### 4.3. Wavelet analysis

The wavelet analysis provides a detailed view of how spectral energy fluctuates over time, offering insights into the dynamic nature of decision-making processes as captured through neurophysiological data. The wavelet power spectrum serves as a quantifiable metric, enabling the precise measurement of these temporal changes [43,62–67].

While the spectra depicted in Figure 2 were computed over the entire 30-second EEG time series, it is important to note that sustained attention is not maintained uniformly throughout this period. To identify specific time windows during which attention was focused, we employed wavelet analysis. Using the Morlet wavelet, we were able to pinpoint intervals where attention was predominantly directed toward one interpretation of the cube over another.

The temporal dynamics of the cube's orientation interpretation were explored through continuous wavelet transform (CWT) analysis, implemented using the Brainstorm software. This method allowed us to investigate how attention shifted over time, revealing the moments when the subject focused attention on specific interpretations of the cube. By leveraging wavelet analysis, we gained a more granular understanding of the temporal patterns underlying attentional processes during the task.

Figures 3(a) and 3(b) depict the variations in wavelet energy corresponding to figurative attention directed towards the left (MLV) and right (MRV) cube orientations, respectively. The wavelet energy was calculated using the following equation:

$$W(f, t) = \sqrt{f} \int_{t-4/f}^{t+4/f} X(t) \psi^*(f, t) dt, \quad (10)$$

where the asterisk (\*) denotes the complex conjugate,  $X(t)$  represents the analyzed EEG signal, and  $\psi(f, t)$  is the complex-valued Morlet wavelet, chosen as the mother wavelet. The Morlet wavelet is defined as:

$$\psi(f, t) = \sqrt{f} \pi^{1/4} e^{i\omega_0 f(t-t_0)} e^{f(t-t_0)^2/2} \quad (11)$$

with  $\omega_0 = 2\pi f_0$  is the central frequency of the Morlet wavelets,  $i = \sqrt{-1}$  is the imaginary unit, and  $t_0$  represents the time shift parameter. This formulation allows for a precise analysis of the temporal and spectral characteristics of the EEG signal, capturing the dynamic shifts in attention during the task.

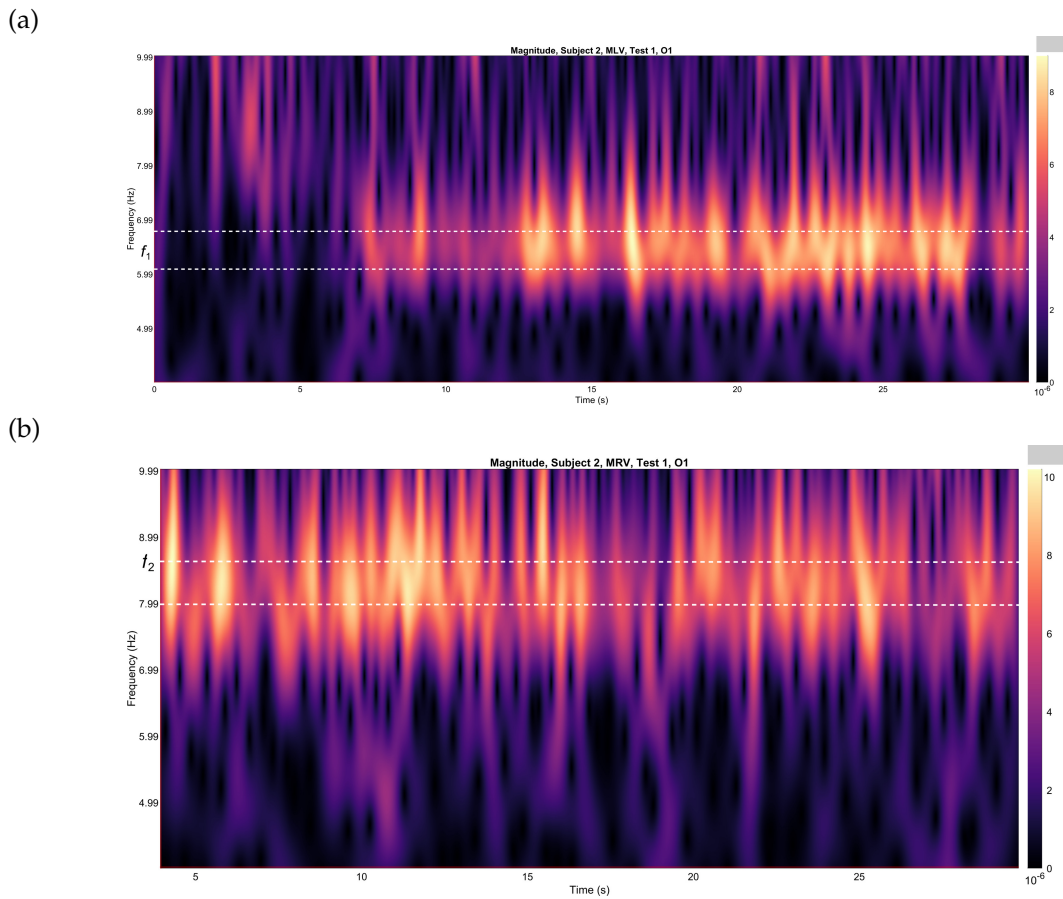


**Figure 3.** Wavelets from channel O1, illustrating the spectral energy associated with figurative attention directed towards (a) left-cube (MLV) and (b) right-cube (MRV) orientations. The peak wavelet energy is observed within distinct frequency regions: (a)  $f_1$  when the subject perceives the cube as left-oriented, and (b)  $f_2$  when the subject perceives the cube as right-oriented. The frequency ranges  $f_1$  and  $f_2$  are demarcated by horizontal dashed lines, highlighting the specific bands where attentional focus is most pronounced.

It is evident that the prominence of specific components corresponds to the subject's directed attention towards either the left or right orientation of the cube. The spectral component at  $f_1$  is dominant when the subject perceives the cube as left-oriented (Fig. 3(a)), while  $f_2$  prevails when the cube is interpreted as right-oriented (Fig. 3(b)). As shown in Figure 3, spectral energy at  $f_1$  dominates during the time interval  $t_L \in [6.88, 28.12]$  seconds in the MLV test, whereas spectral energy at  $f_2$  dominates during the interval  $t_R \in [3.94, 30]$  seconds in the MRV test. In the subsequent analysis, connectivity is calculated within these identified time intervals.

## 5. Graph Construction

In this section, we construct brain connectivity networks associated with figurative attention using three widely used measures: coherence, cross-correlation, and mutual information. These measures allow us to examine how attention influences both connectivity and disconnectivity between different brain regions. During an attentive state, connectivity between some brain areas may increase, while in others, it may decrease. To capture this dynamics, we construct separate graphs for positive and negative connectivity changes.

The connectivity measures  $C = \{Coh, Corr, Inf\}$  were calculated for every pair of signals recorded from 16 EEG channels within the frequency ranges  $6.15 < f_1 < 6.75$  and  $8.00 < f_2 < 8.60$ , as identified from the FFT spectra. Additionally, from the wavelet analysis (Figure 3) we selected time intervals of  $t_L \in [3.94, 30]$  seconds for attention to the left-oriented cube and  $t_R \in [11, 23]$  seconds for attention to the right-oriented cube.

Connectivity  $C$  between brain regions was calculated for signals from each electrode pair using Eqs. (7), (8), and (9) for MI, MLV, and MRV tests in both the  $f_1$  and  $f_2$  spectral regions. Subsequently, we determined positive and negative changes in connectivity associated with attention as follows:

$$\begin{aligned}\Delta C_L(f_1) &= C_{MLV}(f_1) - C_{MI}(f_1), \\ \Delta C_L(f_2) &= C_{MLV}(f_2) - C_{MI}(f_2), \\ \Delta C_R(f_1) &= C_{MRV}(f_1) - C_{MI}(f_1), \\ \Delta C_R(f_2) &= C_{MRV}(f_2) - C_{MI}(f_2).\end{aligned}\quad (12)$$

To evaluate connectivity in the constructed graphs, we utilized the 'conncomp' function in MATLAB. This function identifies connected components in an undirected graph, providing a quantitative measure of network connectivity. It assigns each node a connected component identifier, allowing us to determine the total number of connected components within the graph.

### 5.1. Connectivity Graphs Based on Coherence

To construct connectivity graphs, we first calculate coherence between signals from each pair of electrodes for the MI, MLV, and MRV tests in the  $f_1$  and  $f_2$  spectral regions using Eq. (7). Next, we computed the differences  $\Delta Coh_L$  and  $\Delta Coh_R$  associated with attention using Eq. (12). The resulting labeled graphs of coherence ( $\Delta Coh > 0$ ) and anticoherece ( $\Delta Coh < 0$ ) are displayed in Figures 4 and 5, respectively. The corresponding  $16 \times 16$  coherence matrices are provided in Figures A1 and Figures A2 in Appendix A.

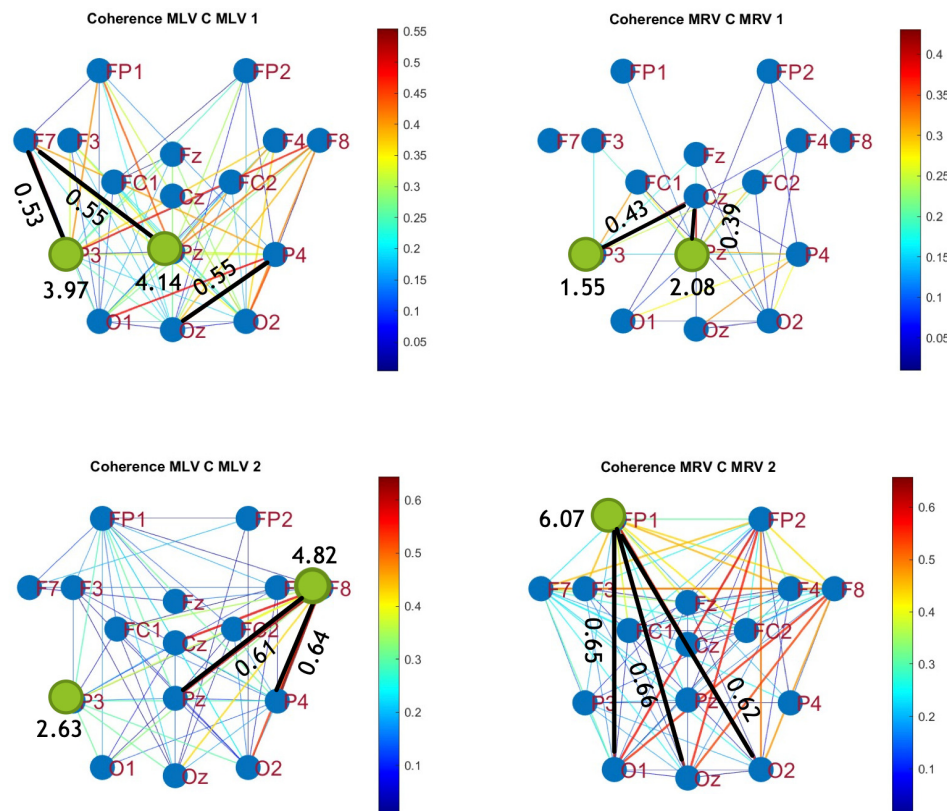


**Figure 4.** Connectivity graphs based on coherence in the (upper row)  $f_1$  and (lower row)  $f_2$  frequency regions, associated with (left column) left-cube attention ( $\Delta Coh_L > 0$ ) and (right column) right-cube attention ( $\Delta Coh_R > 0$ ). Bold lines highlight the links with the largest coherence differences (Max  $\Delta Coh$ ), which are displayed next to the corresponding links. Orange dots denote the nodes with the highest sums of their link weights, indicated next to these nodes.

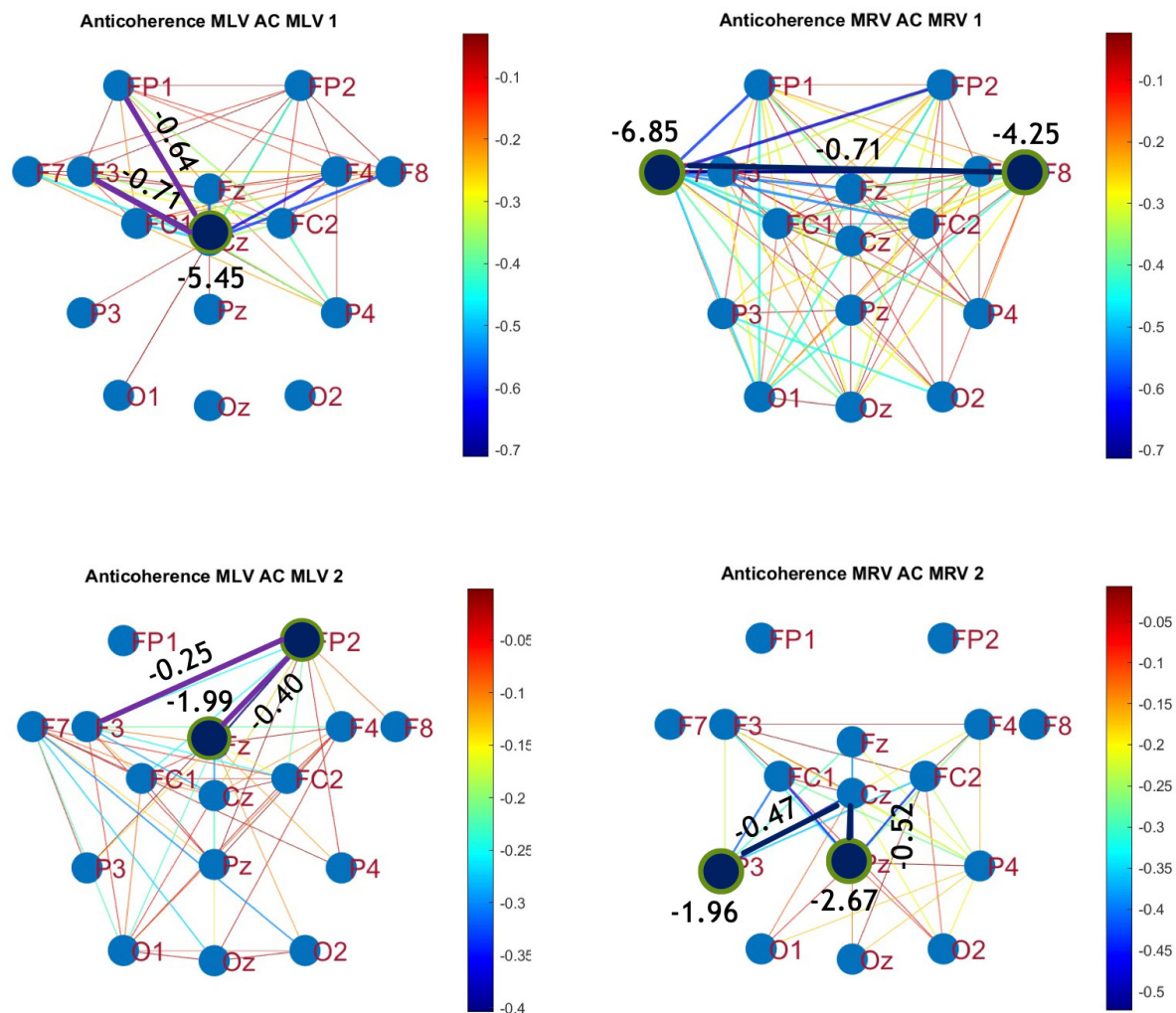


**Figure 5.** Disconnectivity graphs based on anticohereance in the (upper row)  $f_1$  and (lower row)  $f_2$  frequency regions, associated with (left column) left-cube attention ( $\Delta Coh_L < 0$ ) and (right column) right-cube attention ( $\Delta Coh_R < 0$ ). Bold lines highlight the links with the largest negative coherence differences (Min  $\Delta Coh$ ). Violet dots denote the nodes with the lowest sums of their link weights, indicated next to these nodes.

The colors in Figures 4 and 5 represent the numerical weights of the links, illustrating coherence differences ( $\Delta Coh$ ) resulting from shifts in attention. The strongest links are emphasized with bold lines and labeled with their corresponding coherence differences. We also calculated the total sum of link weights for each node, displaying these values next to the nodes with the highest sums, which are marked with orange dots. In contrast, nodes with the lowest (negative) labels are indicated with violet dots.

A significant contrast in coherence patterns emerges between frequency regions  $f_1$  and  $f_2$ . When attention is directed toward the left-cube orientation, coherence increases prominently between the left anterior frontal (F7) and midline parietal (Pz) and left parietal (P3) lobes at  $f_1$  (upper left panel, Figure 4). In contrast, at  $f_2$ , coherence increases symmetrically in the right hemisphere, particularly between the right anterior frontal (F8), midline parietal (Pz), and right parietal (P4) lobes (lower left panel, Figure 4). These findings suggest that the anterior frontal lobes play a crucial role in figurative attention.

For right-cube attention, coherence increases between the left parietal (P3) and midline central (Cz) lobes, as well as between the midline parietal (Pz) and midline central (Fz) lobes at  $f_1$  (upper right panel, Figure 4). However, at  $f_2$ , coherence significantly increases between the occipital cortex (O1, Oz, O2) and the left prefrontal lobe (FP1) (lower right panel, Figure 4). These observations suggest that the left prefrontal cortex may play a key role in processing right-cube orientation, as the frequency  $f_2$



is applied to the right face of the cube. Our findings align with prior studies, such as Al-Nafjan and Aldayel [38], which also reported attention-related activity in the prefrontal and parietal cortices.

A critical aspect of these results is the simultaneous decrease in coherence between certain brain regions, indicating that attention not only strengthens specific neural connections but also selectively disconnects others. Given the brain energy-intensive nature, this redistribution likely reflects an optimization of cognitive resources. Figure 5 visualizes this selective disconnectivity through anticohereance graphs.

The results reveal a notable reduction in coherence at  $f_1$  between the midline central (Cz) and left frontal (F3) lobes, as well as between the midline central (Cz) and left prefrontal (FP1) lobes during left-cube attention (upper left panel, Figure 5). At  $f_2$ , coherence decreases between the midline frontal (Fz) and right prefrontal (FP2) lobes, as well as between the left frontal (F3) and right prefrontal (FP2) lobes (lower left panel, Figure 5). These results suggest that the central cortex is a primary region of disconnectivity and that the reduction in prefrontal-central connectivity facilitates increased parietal-frontal interactions.

For right-cube attention, a different pattern emerges. At  $f_1$ , coherence decreases between the anterior frontal lobes (F7 and F8), while at  $f_2$  coherence decreases between the left parietal (P3) and midline central (Cz) lobes, as well as between the midline parietal (Pz) and midline central (Cz) lobes. Notably, the nodes (P3, Pz) and links to Cz with the greatest coherence reduction at  $f_2$  (lower right panel, Figure 5) coincide with those showing the greatest coherence increase at  $f_1$  (upper right panel, Figure 4). This suggests a frequency-dependent reorganization, where attention to the right-cube orientation enhances coherence in these regions at  $f_1$  while simultaneously reducing coherence at  $f_2$ .

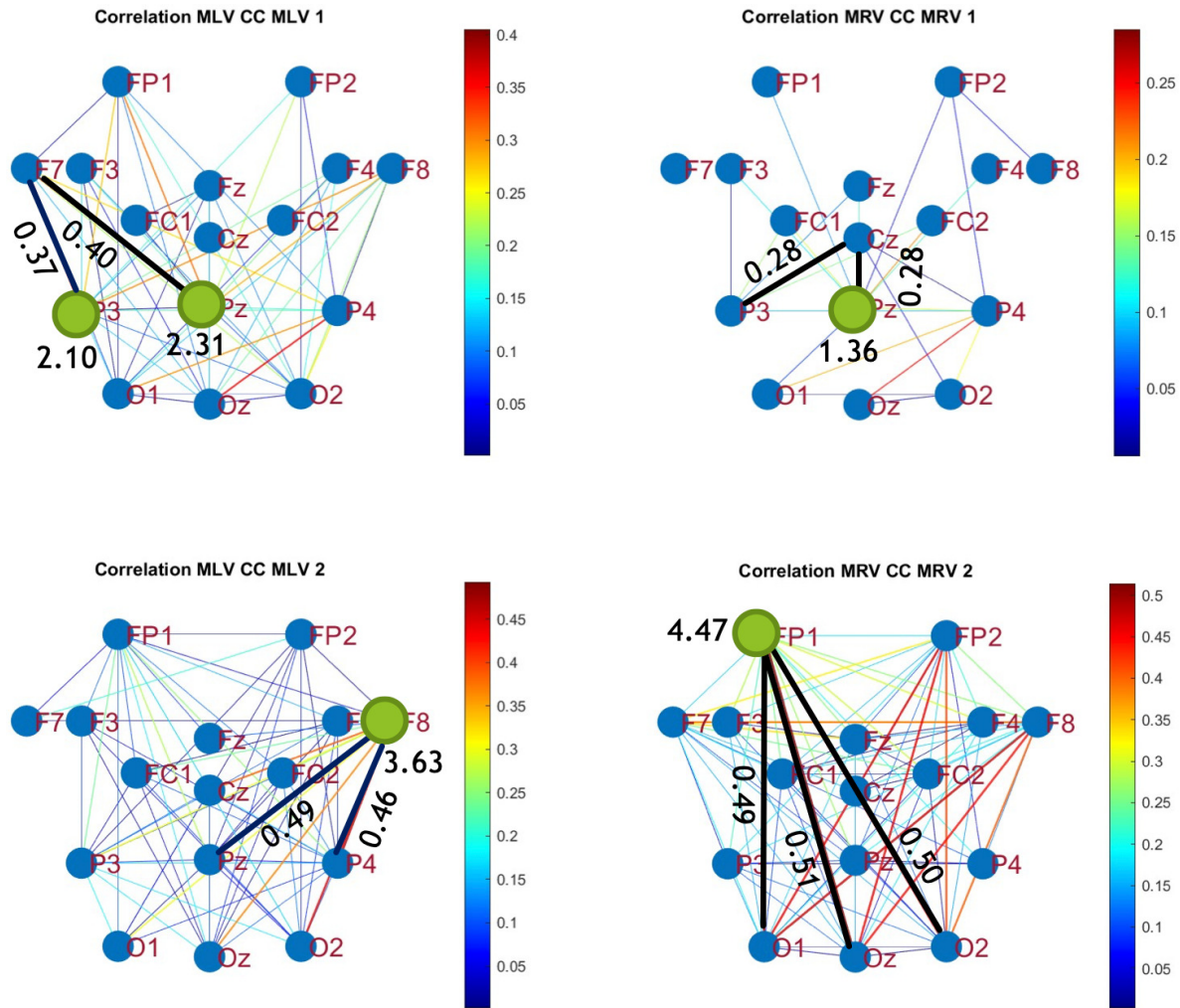
Table 1 summarizes the graph-based analysis of brain connectivity, listing the two highest positive and negative coherence differences (link weights) and their corresponding lobes.

Table 1. Maxima and minima coherence differences.

Measure	Value	Lobes	Value	Lobes
Max $\Delta Coh_L(f_1)$	0.55	F7 – Pz	0.53	F7 – P3
Max $\Delta Coh_L(f_2)$	0.64	F8 – P4	0.61	F8 – Pz
Max $\Delta Coh_R(f_1)$	0.43	Cz – P3	0.39	Cz – Pz
Max $\Delta Coh_R(f_2)$	0.66	Oz – FP1	0.65	O1 – FP1
Min $\Delta Coh_L(f_1)$	−0.64	Cz – FP1	−0.71	Cz – F3
Min $\Delta Coh_L(f_2)$	−0.40	Fz – FP2	−0.25	F3 – FP2
Min $\Delta Coh_R(f_1)$	−0.71	F7 – F8	−0.66	F7 – F4
Min $\Delta Coh_R(f_2)$	−0.52	Pz – Cz	−0.47	P3 – Cz

5.2. Connectivity Graphs Based on Cross-Correlation

To construct connectivity graphs based on cross-correlation, we first computed cross-correlation between EEG signals from each pair of channels using Eq. (8), then calculated attention-induced differences using Eq. (12). The resulting graphs, shown in Figures 6 and 7, depict regions of the increasing and decreasing cross-correlation, respectively. Additionally, the corresponding cross-correlation matrices, presented in Appendix A (Figures A3 and A4), provide a detailed numerical representation of these connectivity changes.



**Figure 6.** Connectivity graphs based on cross-correlation in the (upper row)  $f_1$  and (lower row)  $f_2$  frequency regions, associated with (left column) left-cube attention ( $\Delta Corr_L > 0$ ) and (right column) right-cube attention ( $\Delta Corr_R > 0$ ). Bold lines highlight the links with the largest correlation differences (Max  $\Delta Corr$ ), which are displayed next to the corresponding links. Orange dots denote the nodes with the highest sums of their link weights, indicated next to these nodes.

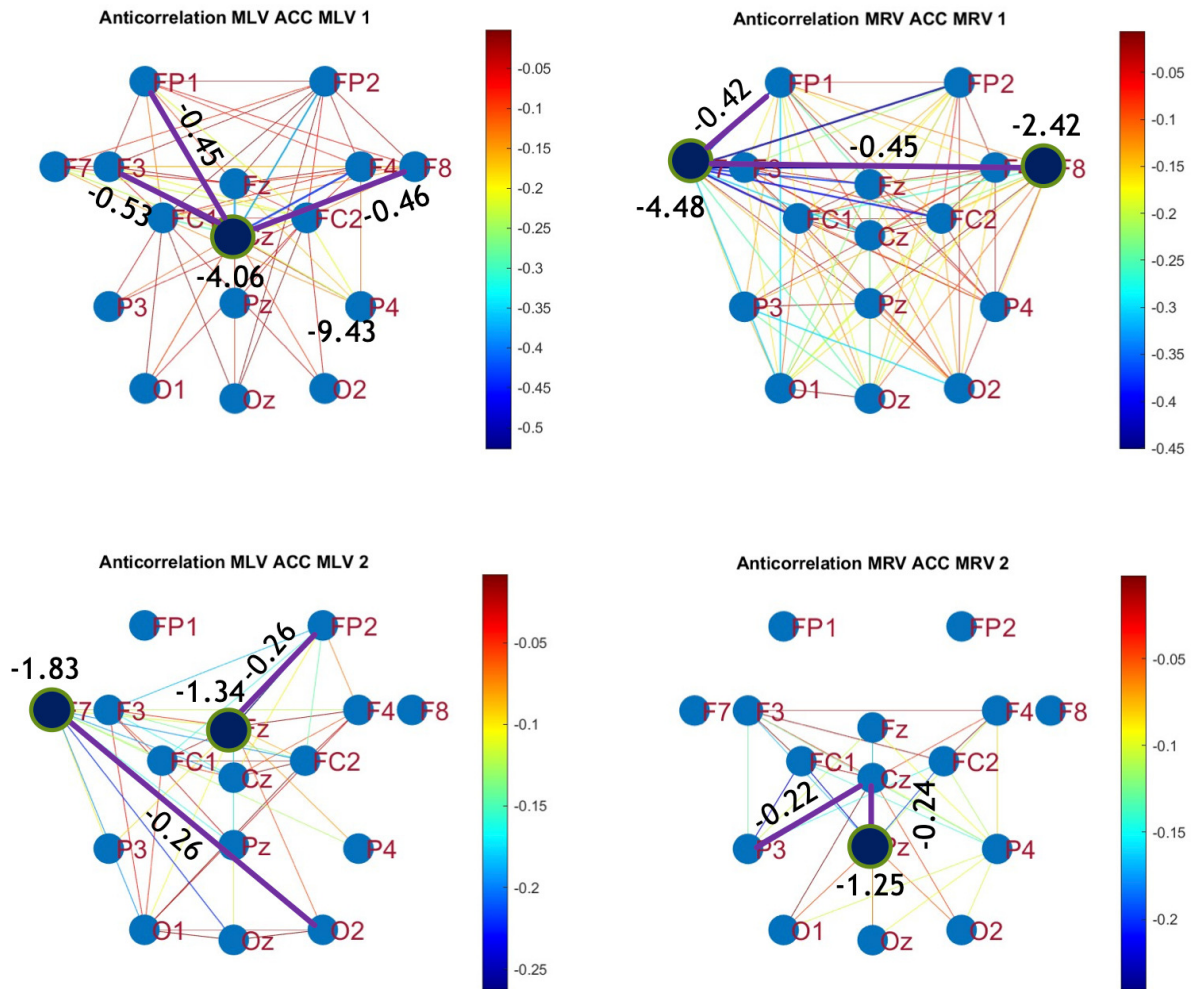


**Figure 7.** Disconnectivity graphs based on anticorrelation in the (upper row)  $f_1$  and (lower row)  $f_2$  frequency regions, associated with (left column) left-cube attention ( $\Delta Corr_L < 0$ ) and (right column) right-cube attention ( $\Delta Corr_R < 0$ ). Bold lines highlight the links with the largest negative cross-correlation differences (Min  $\Delta Corr$ ). Violet dots denote the nodes with the lowest sums of their link weights, indicated next to these nodes.

By comparing Figures 4 and 5 with Figures 6 and 7, we observe a strong similarity between the connectivity patterns derived from cross-correlation and coherence measures. Specifically, the links showing the maximum increases and decreases in cross-correlation closely match those for coherence. This agreement between connectivity measures, based on both temporal and spectral analyses, provides strong validation for the robustness of our findings.

Table 2 summarizes the results of the brain connectivity analysis based on cross-correlation. The table presents the two largest positive and negative correlation differences (link weights) along with the corresponding brain regions.

**Table 2.** Maxima and minima cross-correlation differences.

Measure	Value	Lobes	Value	Lobes
Max $\Delta Corr_L(f_1)$	0.40	F7 – Pz	0.37	F7 – P3
Max $\Delta Corr_L(f_2)$	0.49	F8 – Pz	0.46	F8 – P4
Max $\Delta Corr_R(f_1)$	0.28	P3 – Cz	0.28	Pz – Cz
Max $\Delta Corr_R(f_2)$	0.51	Oz – FP1	0.51	O2 – FP1
Min $\Delta Corr_L(f_1)$	–0.53	Cz – F3	–0.45	Cz – FP1
Min $\Delta Corr_L(f_2)$	–0.26	Fz – FP2	–0.26	O2 – F7
Min $\Delta Corr_R(f_1)$	–0.45	F7 – F8	–0.42	F7 – FP1
Min $\Delta Corr_R(f_2)$	–0.24	Pz – Cz	–0.22	P3 – Cz

### 5.3. Connectivity Graphs Based on Mutual Information

The third connectivity measure explored in this study, mutual information, was calculated using Eq. (9). The differences in mutual information induced by attention were computed using Eq. (12). The resulting graphs depicting the attention-induced changes in mutual information are shown in Figures 8 and 9. Additionally, the corresponding mutual information matrices are provided in Appendix A, specifically in Figures A5 and A6, offering a detailed numerical representation of these connectivity changes.

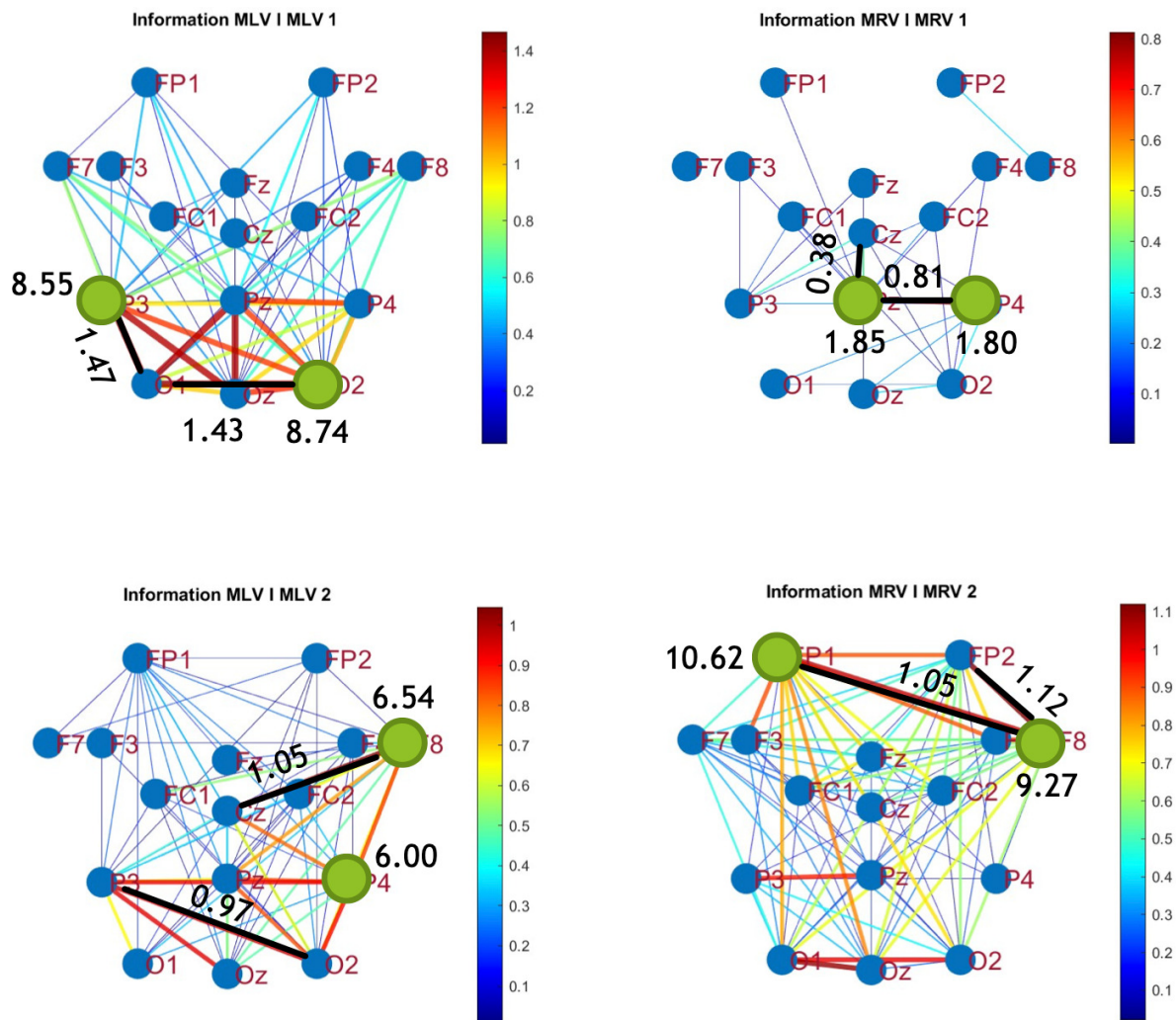


**Figure 8.** Connectivity graphs based on mutual information in the (upper row)  $f_1$  and (lower row)  $f_2$  frequency regions, associated with (left column) left-cube attention ( $\Delta Inf_L > 0$ ) and (right column) right-cube attention ( $\Delta Inf_R > 0$ ). Bold lines highlight the links with the largest mutual information differences (Max  $\Delta Inf$ ), which are displayed next to the corresponding links. Orange dots denote the nodes with the highest sums of their link weights, indicated next to these nodes.



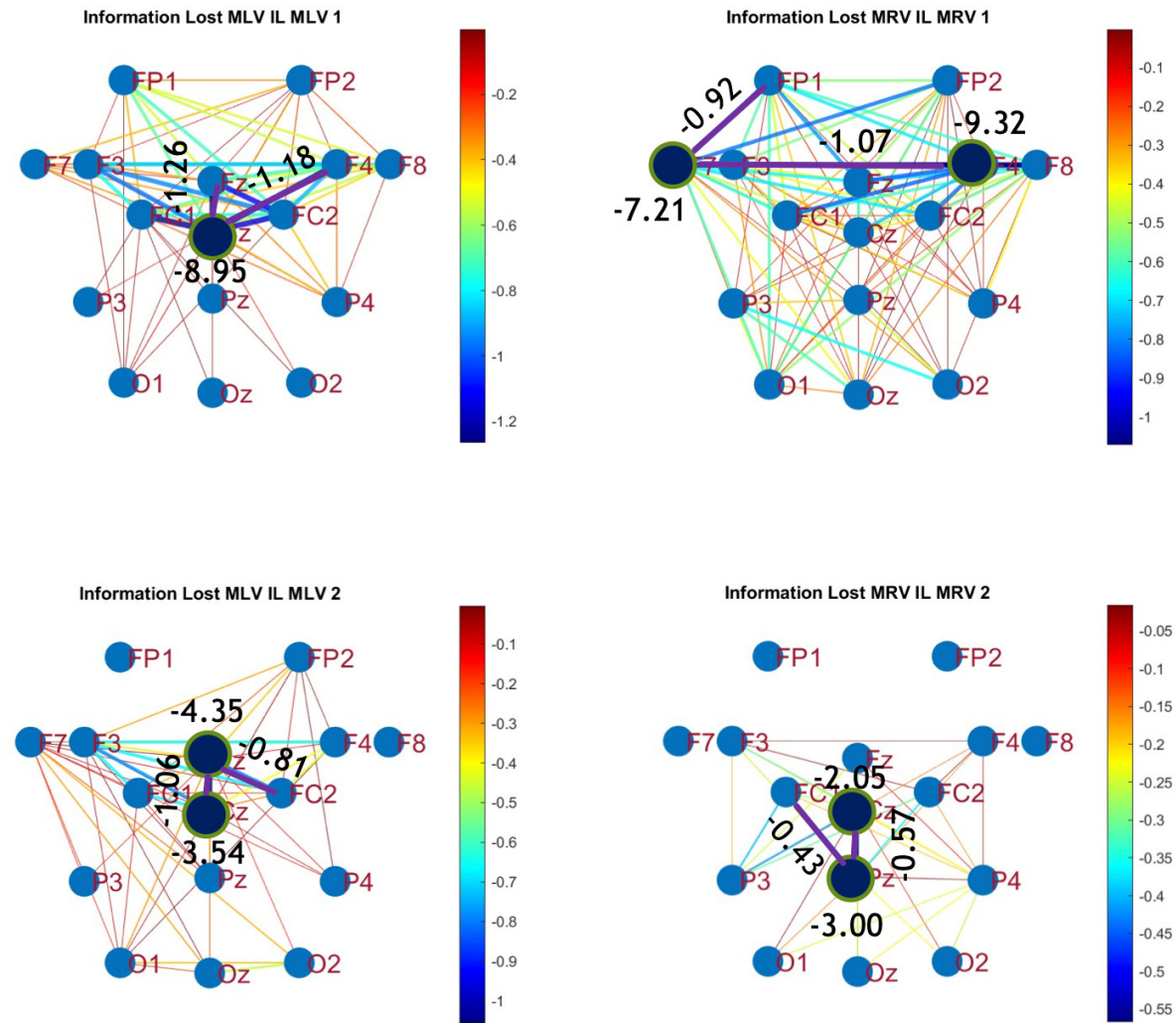


**Figure 9.** Disconnectivity graphs based on mutual information loss in the (upper row)  $f_1$  and (lower row)  $f_2$  frequency regions, associated with (left column) left-cube attention ( $\Delta Inf_L < 0$ ) and (right column) right-cube attention ( $\Delta Inf_R < 0$ ). Bold lines highlight the links with the largest negative mutual information differences (Min  $\Delta Inf$ ). Violet dots denote the nodes with the lowest sums of their link weights, indicated next to these nodes.

Table 3 summarizes the brain connectivity analysis results based on mutual information. It highlights the two largest positive and negative mutual information differences (link weights) along with their corresponding brain regions, providing insight into the most significant connectivity changes induced by attention shifts.

**Table 3.** Maxima and minima mutual information differences.

Measure	Value	Lobes	Value	Lobes
Max $\Delta Inf_L(f_1)$	1.41	O1 – P3	1.43	O1 – O2
Max $\Delta Inf_L(f_2)$	1.05	Cz – F3	0.97	O2 – P3
Max $\Delta Inf_R(f_1)$	0.81	P4 – Pz	0.38	Pz – Cz
Max $\Delta Inf_R(f_2)$	1.12	F8 – FP2	1.05	F8 – FP1
Min $\Delta Inf_L(f_1)$	–1.26	Cz – Fz	–1.18	Cz – F4
Min $\Delta Inf_L(f_2)$	–1.06	Cz – Fz	–0.81	Cz – FC2
Min $\Delta Inf_R(f_1)$	–1.07	F7 – F4	–0.92	F7 – FP1
Min $\Delta Inf_R(f_2)$	–0.57	Pz – Cz	–0.22	Pz – FC1

A strong correspondence can be observed among the connectivity graphs based on coherence, cross-correlation, and mutual information. Although some variations exist in the links with the highest

weights, the nodes with the maximum and minimum labels largely overlap across all connectivity measures. This consistency further validates the robustness of our approach in capturing attention-related connectivity changes in the brain.

The shared features across different connectivity measures can be explored using hypergraphs. In the following section, we describe the process of constructing attention hypergraphs.

6. Hypergraph Construction

Hypergraph analysis provides a simplified and more generalized representation of the brain network. Instead of relying on the twelve individual graphs presented in the previous section, we can construct four hypergraphs using the summarization technique described in Sec. 2.2.

To construct the hypergraphs, we follow these steps:

1. Compute the label of every node  $i$  for each connectivity measure  $\Delta C$  using Eq. (2) ( $\text{Lab } C_i = \sum_i^n \Delta C$ ).
2. From probability distribution of all  $n$  labels for each connectivity measure found the mean  $M = \frac{1}{n} \sum_i^n \text{Lab } C_i$  and standard deviation  $\sigma$ .
3. Calculate threshold value  $C_{th} = M \pm \sigma$  for each connectivity measure ("+" for  $M > 0$ , "-" for  $M < 0$ ).
4. Using the threshold value, determine whether a change in connectivity is significant or not. The change is significant if the label  $|\text{Lab } C_i| > |C_{th}|$ .
5. Using the summarization technique described in Sec. 2.2 remove insignificant nodes whose labels are smaller than the threshold value. Weak changes in connectivity is considered as brain noise and not related to attention.
6. Construct incident matrices using Eq. (5).

The probability distributions for each connectivity measure are presented in Figures A7–A9 in Appendix B. One can also find there the values of means ( $M$ ), standard deviations ( $\sigma$ ), and thresholds ( $C_{th}$ ) which are summarized in Table A1.

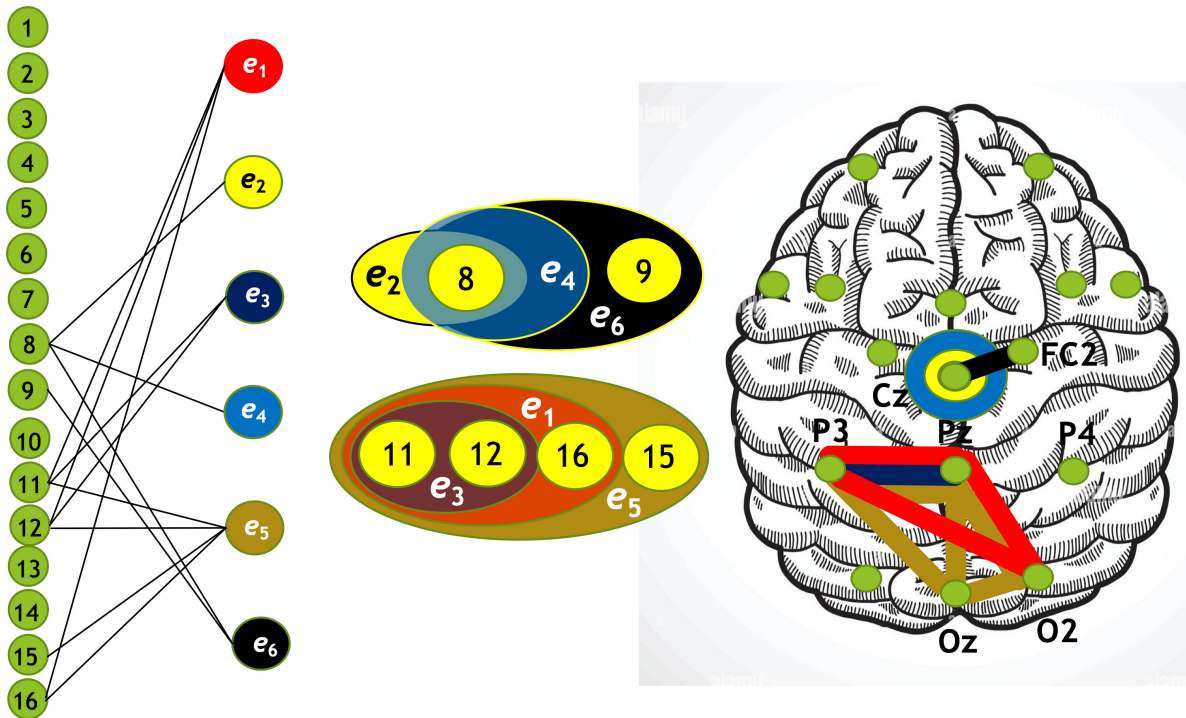
Using the algorithm described above, we constructed four hypergraphs, denoted as  $\mathbf{H}_{1-4}$ . Two of these hypergraphs ( $\mathbf{H}_{1,2}$ ) correspond to attention directed toward the left-cube orientation, while the other two ( $\mathbf{H}_{3,4}$ ) correspond to attention directed toward the right-cube orientation. Hypergraphs  $\mathbf{H}_1$  and  $\mathbf{H}_3$  are constructed for frequency region  $f_1$ , while  $\mathbf{H}_2$  and  $\mathbf{H}_4$  are constructed for  $f_2$ .

Each hypergraph contains six hyperedges ( $m = 6$ ):  $e_1$  and  $e_2$  represent coherence and anticoherence,  $e_3$  and  $e_4$  represent correlation and anticorrelation, and  $e_5$  and  $e_6$  represent mutual information and information loss, respectively.

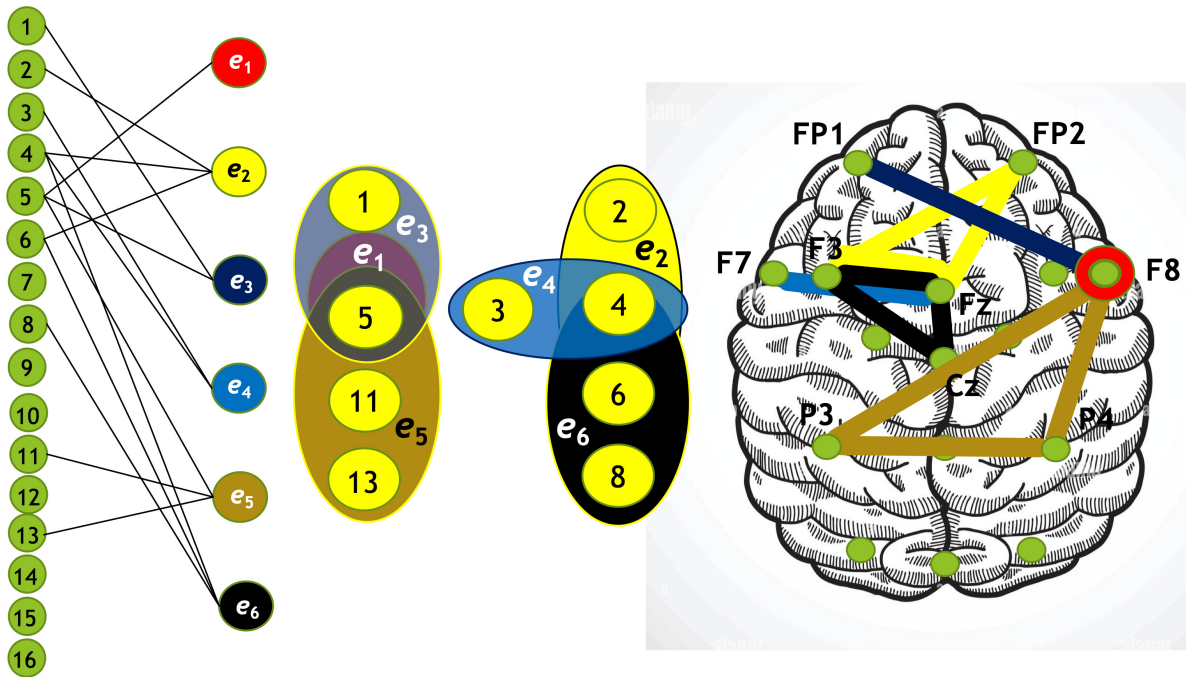
The constructed hypergraphs  $\mathbf{H}_{1-4}$  are visualized in Figures 10–13 in three distinct forms: as a bipartite graph (left panels), a Venn diagram (middle panels), and a brain map (right panels). The correspondence between node numbers and EEG channels is provided in Table 4.

Table 4. Correspondence of node numbers to EEG channels.

1	2	3	4	5	6	7	8	9	10	11	12	13	14	15	16
FP1	FP2	F7	Fz	F8	F3	FC1	Cz	FC2	F4	P3	Pz	P4	O1	Oz	O2



**Figure 10.** Hypergraph  $H_1$  associated with left-cube attention for  $f_1$ , presented as a bipartite graph (left), a Venn diagram (middle), and a brain map (right). The upper Venn diagram ( $e_2, e_4, e_6$ ) indicates deactivation of central area, while the lower one ( $e_1, e_3, e_5$ ) depicts activation of occipital-parietal area.



**Figure 11.** Hypergraph  $H_2$  associated with left-cube attention for  $f_2$ , presented as a bipartite graph (left), a Venn diagram (middle), and a brain map (right). The right Venn diagram ( $e_2, e_4, e_6$ ) indicates deactivation of left frontal and right prefrontal lobes, while the left one ( $e_1, e_3, e_5$ ) depicts activation of parietal, right anterior, and left prefrontal lobes.

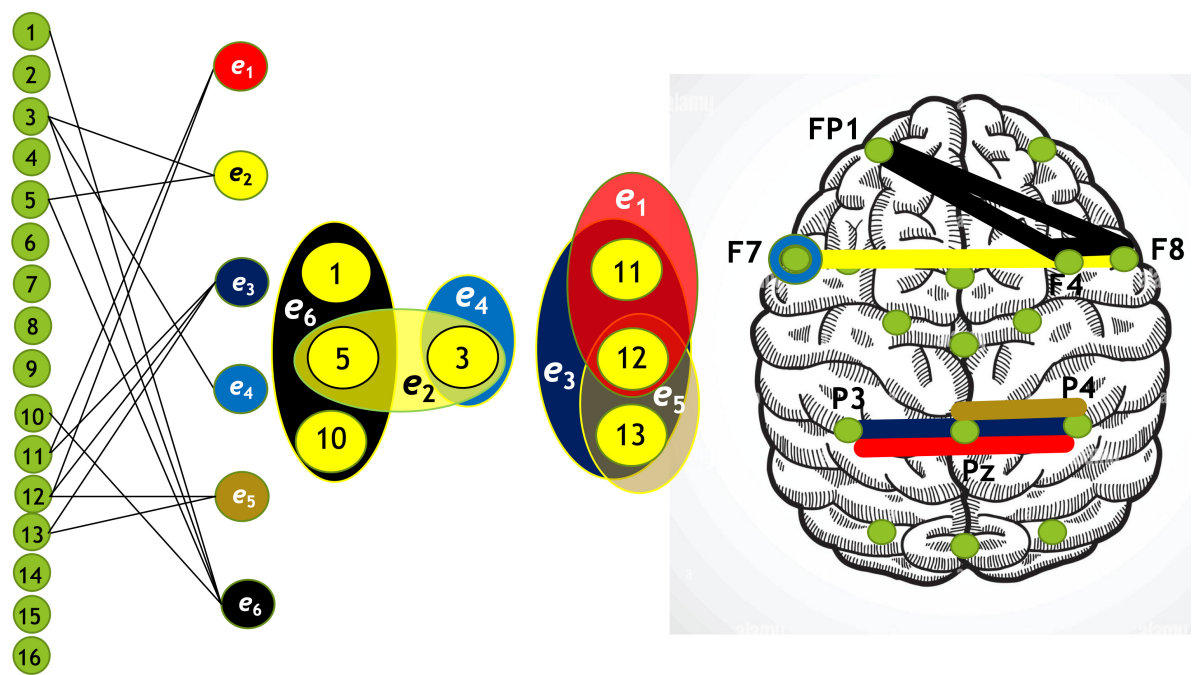


**Figure 12.** Hypergraph  $H_3$  associated with right-cube attention for  $f_1$ , presented as a bipartite graph (left), a Venn diagram (middle), and a brain map (right). The left Venn diagram ( $e_2, e_4, e_6$ ) indicates deactivation of frontal cortex, while the right one ( $e_1, e_3, e_5$ ) depicts activation of parietal area.

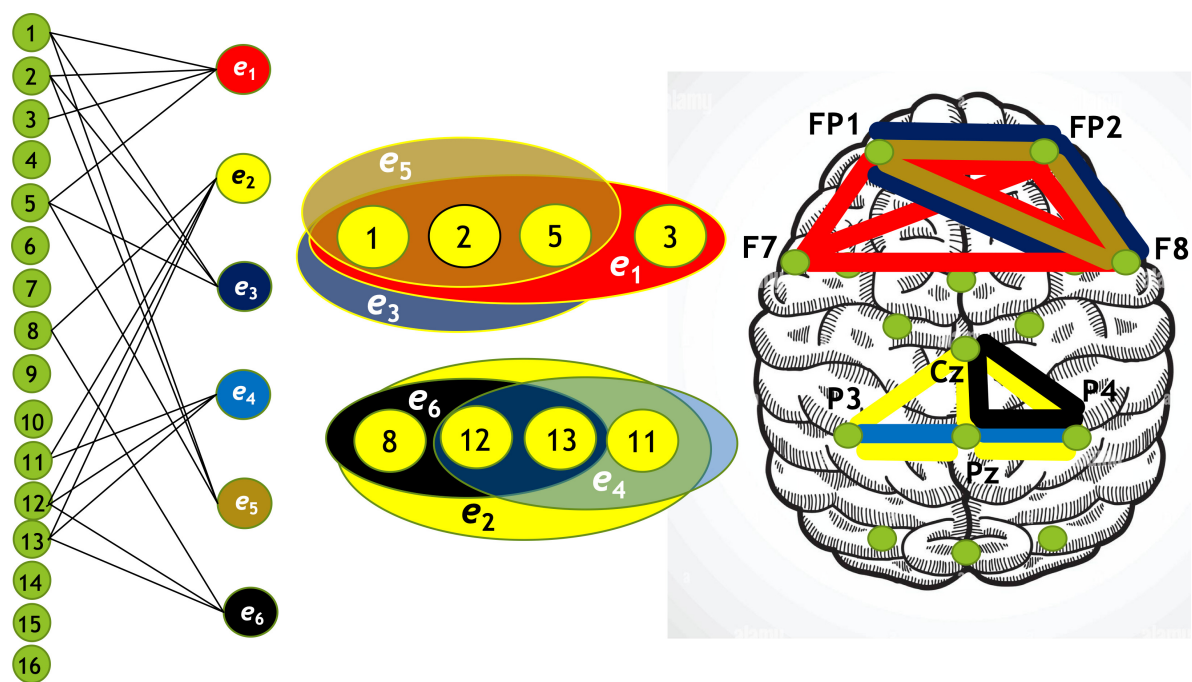


**Figure 13.** Hypergraph  $H_4$  associated with right-cube attention for  $f_2$ , presented as a bipartite graph (left), a Venn diagram (middle), and a brain map (right). The lower Venn diagram ( $e_2, e_4, e_6$ ) indicates deactivation of central-parietal area, while the upper one ( $e_1, e_3, e_5$ ) depicts activation of frontal cortex.

A hypergraph size is the number of hyperedges (in our case  $m = 6$ ), and the order of a hypergraph is the number of vertices. The degrees of hyperedges and the orders of the hypergraphs are summarized in Table 5.



Table 5. Degrees of hyperedges and orders of hypergraphs.

Measure	Hyperedge	H <sub>1</sub> (Left $f_1$ )	H <sub>2</sub> (Left $f_2$ )	H <sub>3</sub> (Right $f_1$ )	H <sub>4</sub> (Right $f_2$ )
Coherence	$e_1$	3	1	3	4
Anticoherence	$e_2$	1	3	2	4
Correlation	$e_3$	2	2	3	4
Anticorrelation	$e_4$	1	2	1	3
Mut. Inform.	$e_5$	4	3	1	3
Inform. Loss	$e_6$	2	3	2	2
Order		6	9	7	8

7. Discussion

Hypergraphs have been extensively studied and applied in network analysis, including node classification [68], community detection [69], and link prediction [70]. In neuroscience, hypergraphs, as a generalization of the graph theory, provide a more sophisticated framework for modeling brain connectivity by capturing high-order interactions among multiple brain regions [71]. Recent studies [33] have constructed hypergraphs using functional and structural connectivity as hyperedges. In contrast, we created hypergraphs based on three connectivity measures (coherence, cross-correlation, and mutual information) and three disconnectivity measures (anticoherence, anticorrelation, and information loss). Additionally, we employed sparsification techniques to remove less significant nodes, reducing noise and enhancing functional connectivity interpretation.

By incorporating hypergraph theory into EEG-based functional connectivity analysis, our method provides a novel perspective on understanding attention and its neural correlates. Hypergraph-based models enable a subject-level representation of high-order relationships, facilitating a more refined analysis of individual differences in cognitive function. This has significant implications for identifying biomarkers of attention-related disorders, such as ADHD, and advancing personalized cognitive assessments. Recent advancements in deep learning have further amplified the potential of hypergraph-based models. Ji et al. [19] introduced the hypergraph attention network (FC-HAT), while Bi et al. [72] developed the hypergraph structural information aggregation generative adversarial network (HSIA-GAN) model for functional connectivity analysis. These models dynamically construct functional connectivity networks, extract abnormal connectivity patterns, and identify critical biomarkers for neurodevelopmental and neurodegenerative disorders.

Our hypergraph analysis reveals that hyperedges associated with increased and decreased connectivity are spatially distinct and localized in different brain regions, depending on both the cognitive task and frequency. Since attention to the left-cube orientation is linked to increased spectral energy at  $f_1$ , the hypergraph in Figure 10 highlights the key nodes involved in this cognitive process. Notably, the occipital-parietal cortex emerges as a central hub for functional connectivity, whereas the central cortex plays a predominant role in disconnectivity.

An intriguing observation is the frequency-dependent nature of brain region activity: nodes that exhibit increased connectivity at one frequency tend to show decreased connectivity at another. For instance, the left parietal lobe (P3), which is highly active at  $f_1$  (Figure 10), demonstrates reduced activity at  $f_2$  (Figure 11), suggesting a dynamic reconfiguration of neural networks in response to different attentional states.

A similar pattern is evident during right-cube attention. The hypergraph in Figure 13 indicates that the frontal cortex plays a central role in connectivity, while the central-parietal cortex is predominantly associated with disconnectivity. This observation aligns with the fact that right-cube attention corresponds to increased spectral energy at  $f_2$ . Once again, the same brain regions exhibit frequency-dependent activation and deactivation, reinforcing the notion that attentional shifts are accompanied by distinct neural reorganization patterns across different frequency bands. Specifically, for right-cube attention, the frontal and prefrontal cortices demonstrate increased activity at  $f_2$  (Figure



13) but reduced activity at  $f_1$  (Figure 12). In contrast, the parietal cortices show the opposite trend, increasing their activity at  $f_1$  (Figure 12) while decreasing at  $f_2$  (Figure 13).

These findings suggest that figurative attention involves a dynamic redistribution of neural resources, with specific brain regions alternating between connectivity and disconnectivity depending on the cognitive demand and frequency. This underscores the importance of considering frequency-specific interactions when analyzing functional brain connectivity and highlights the potential of hypergraph-based approaches for capturing the complexity of attentional processes.

## 8. Conclusion

This study presents a comprehensive hypergraph-based analysis of functional brain connectivity during figurative attention to an ambiguous visual stimulus, integrating coherence, cross-correlation, and mutual information from EEG data. Our findings support the hypothesis that figurative attention engages cortico-cortical interactions, with hypergraph representations revealing distinct frequency-dependent activation and deactivation patterns across brain regions. Notably, the parietal, frontal, and prefrontal lobes play a key role in integrating information, highlighting their functional specialization and dynamic reconfiguration in attentional processing. However, while these regions facilitate efficient cognitive functions, some information may be lost in the central cortex, underscoring the complexity of neural information processing.

By leveraging a frequency-tagging approach in the context of the Necker cube illusion, we identified distinct connectivity patterns corresponding to different cube orientations. Our results emphasize the role of bilateral cortico-cortical interactions and suggest the existence of integrated processing hubs that coordinate visual attention. Hypergraph analysis, extending beyond traditional graph-based methods, provided novel insights into higher-order relationships between multiple brain regions, offering a more comprehensive understanding of dynamic neural interactions.

The methodology developed in this study—incorporating three connectivity and three disconnectivity measures—enabled the identification of higher-order relationships among brain regions, facilitating a more precise characterization of functional connectivity networks underlying figurative attention. This multivariate approach allowed us to construct connectivity difference matrices, revealing both new connections induced by sustained attention and disconnections due to decreased connectivity. Additionally, by applying a sparsification method based on statistical thresholds, we filtered out spurious or noisy connections, enhancing the robustness and interpretability of our functional connectivity network.

Beyond its theoretical implications, this methodological framework holds promise for practical applications in cognitive neuroscience, attention monitoring, and the clinical assessment of attention-related disorders. While this proof-of-concept study is based on a single subject, it establishes a foundation for future large-scale investigations into the neural mechanisms underlying ambiguous visual perception and attentional control.

Although previous studies have explored frequency correlations and proposed biophysical models of neural interactions, our findings highlight the need for further studies investigating the mechanisms linking different frequency-dependent processes. A more refined hypergraph analysis, focusing on smaller neural ensembles or specific regions of interest, could provide deeper insights into the intricate dynamics of brain connectivity. This study lays essential groundwork for advancing our understanding of brain network dynamics and their role in cognitive function.

Hypergraphs provide a powerful framework for modeling high-order interactions in EEG-based functional connectivity networks. Our findings emphasize the importance of incorporating connectivity and disconnectivity measures in hypergraph construction, enabling a more comprehensive understanding of individual differences in attention and cognitive processing. Future research should focus on further refining hypergraph learning algorithms, integrating dynamic hypergraph representations, and expanding applications to clinical populations for biomarker discovery and personalized interventions in cognitive and psychiatric disorders.

Despite these promising findings, substantial challenges remain in translating this approach into clinical practice, including the need for larger datasets, improved interpretability of hypergraph-based models, and validation across diverse cognitive tasks. Nevertheless, our study represents a significant step toward more accurate and individualized assessments of brain function, paving the way for future advancements in cognitive neuroscience and clinical diagnostics.

**Data Availability Statement:** The data presented in this study are openly available in Google Drive at [https://drive.google.com/drive/folders/1\\_PHVe2rsr4ohWufccE7oYNKNAEOB37BA](https://drive.google.com/drive/folders/1_PHVe2rsr4ohWufccE7oYNKNAEOB37BA).

**Author Contributions:** A.N.P.: conceptualization, methodology, investigation, formal analysis, validation, visualization, writing – original draft preparation, supervision; N.P.S.: investigation, formal analysis, visualization; W.E.P.: investigation, data curation, software; R.J.R.: investigation, validation, review and editing.

**Conflicts of Interest:** The authors declare no conflicts of interest.

## Appendix A. Connectivity Matrices

The matrices of the explored connectivity measures are presented in Figures A1–A6.

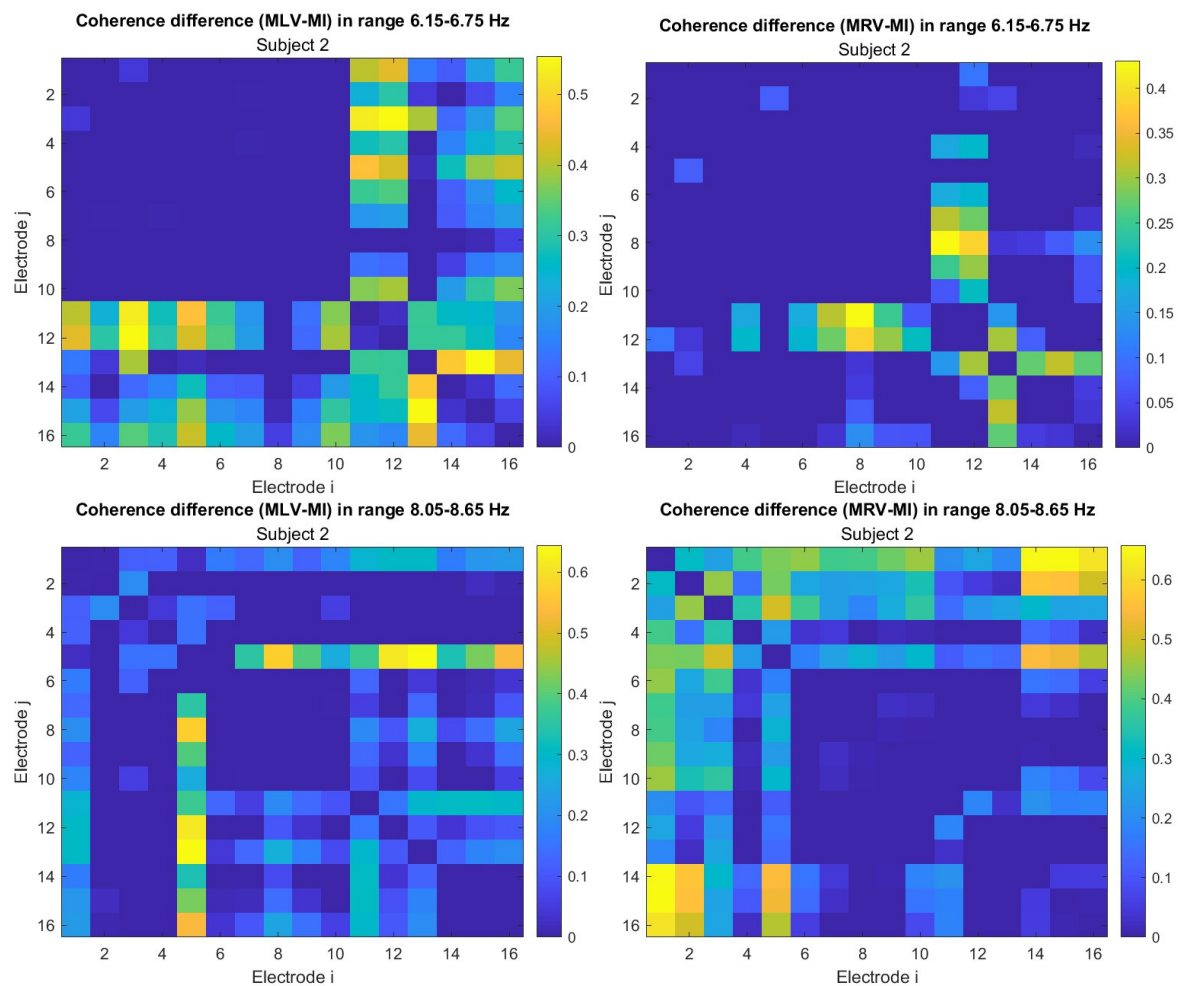


**Figure A1.** Increasing coherence ( $\Delta Coh > 0$ ) associated with figurative attention to (left panels) left cube orientation and (right panels) at frequencies (upper raw)  $f_1$  and (lower raw)  $f_2$ .

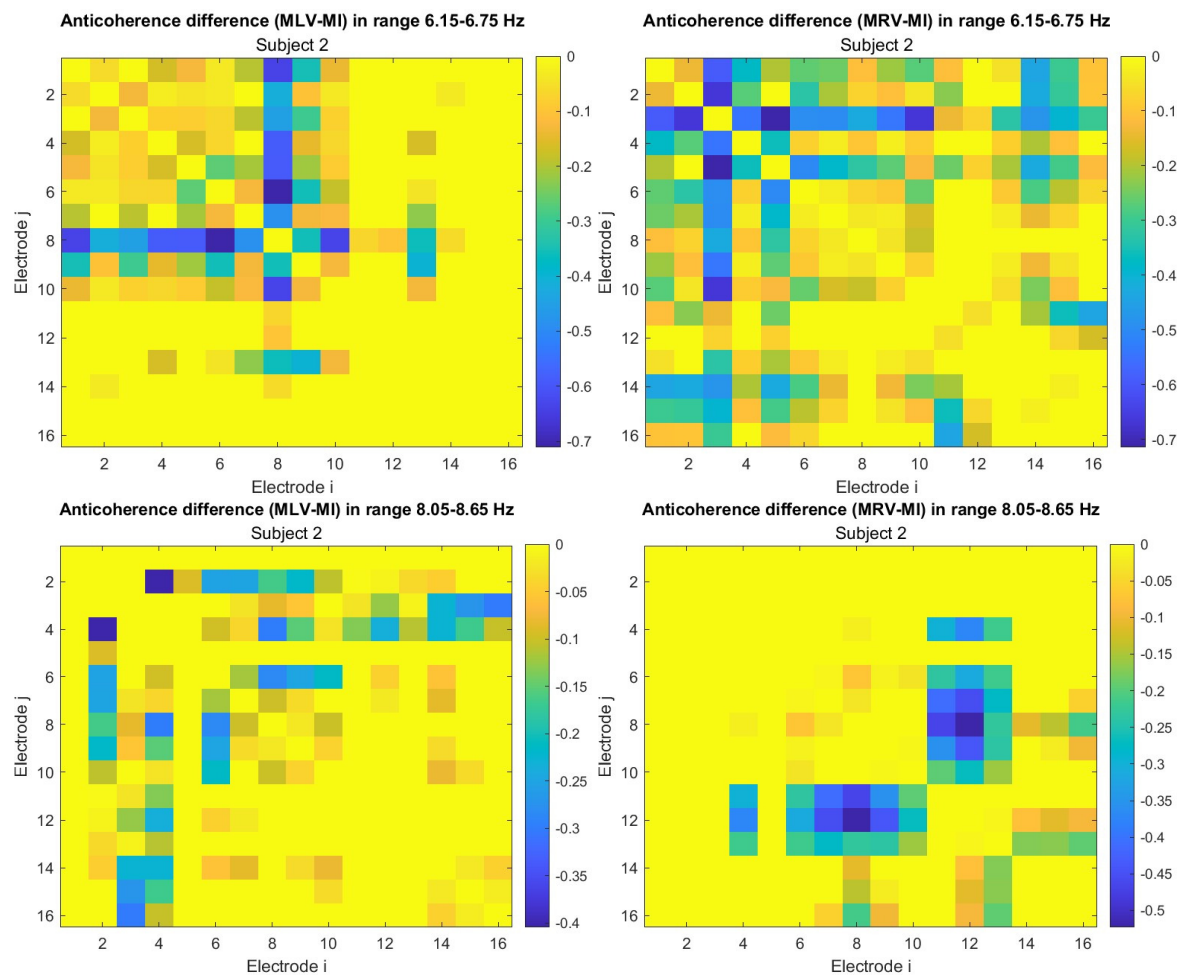


**Figure A2.** Decreasing coherence ( $\Delta Coh < 0$ ) associated with figurative attention to (left panels) left cube orientation and (right panels) at frequencies (upper row)  $f_1$  and (lower row)  $f_2$ .

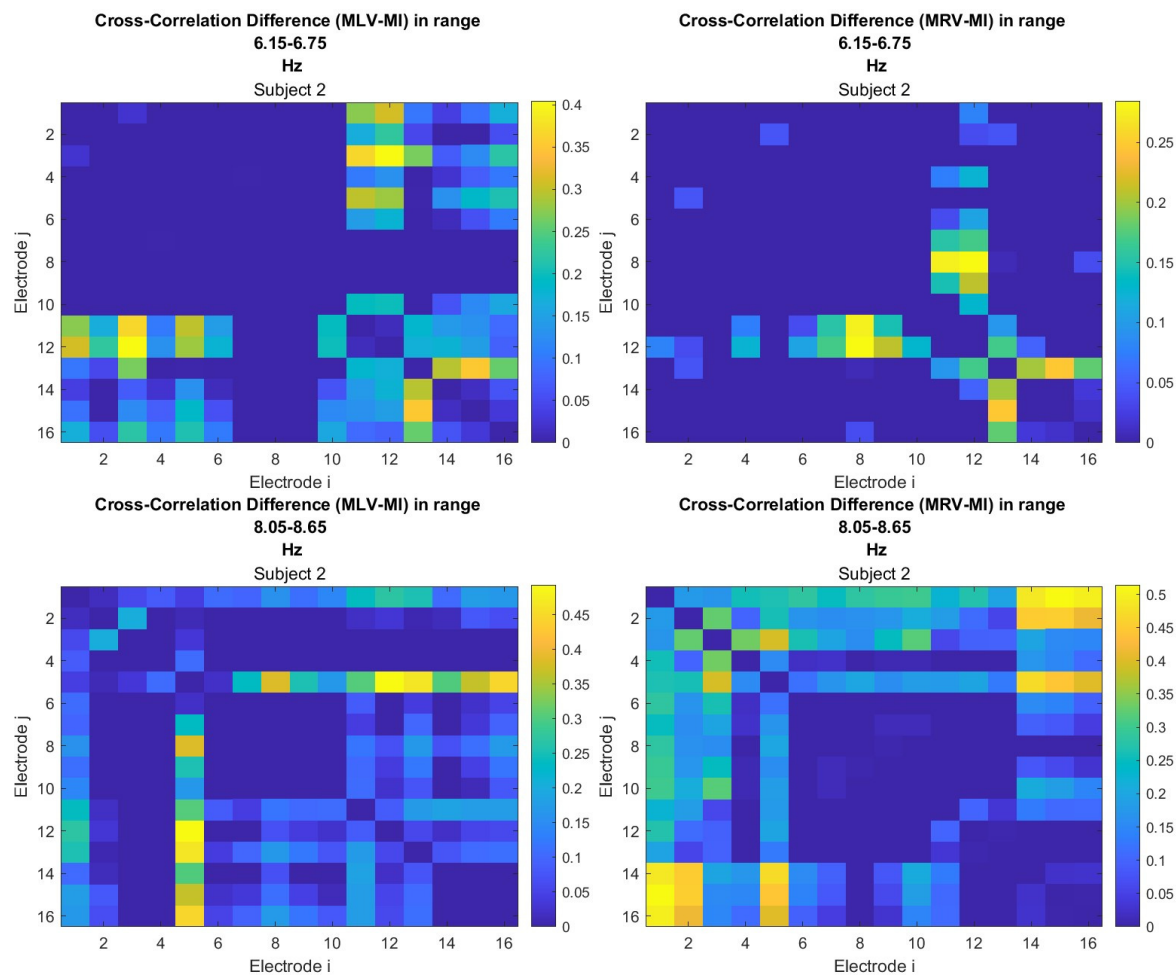


**Figure A3.** Increasing cross-correlation ( $\Delta Corr > 0$ ) associated with figurative attention to (left panels) left cube orientation and (right panels) at frequencies (upper row)  $f_1$  and (lower row)  $f_2$ .

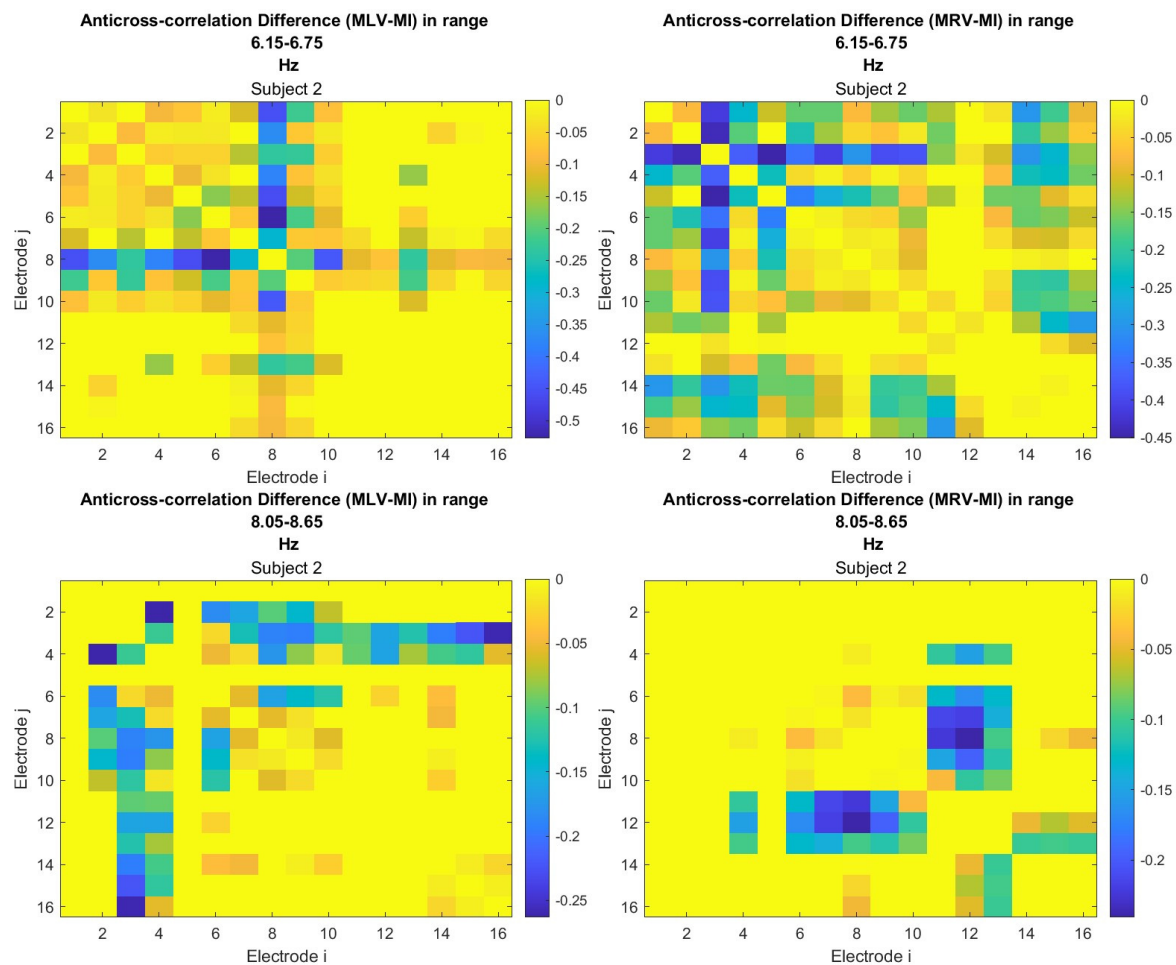


**Figure A4.** Decreasing cross-correlation ( $\Delta Corr < 0$ ) associated with figurative attention to (left panels) left cube orientation and (right panels) at frequencies (upper raw)  $f_1$  and (lower raw)  $f_2$ .



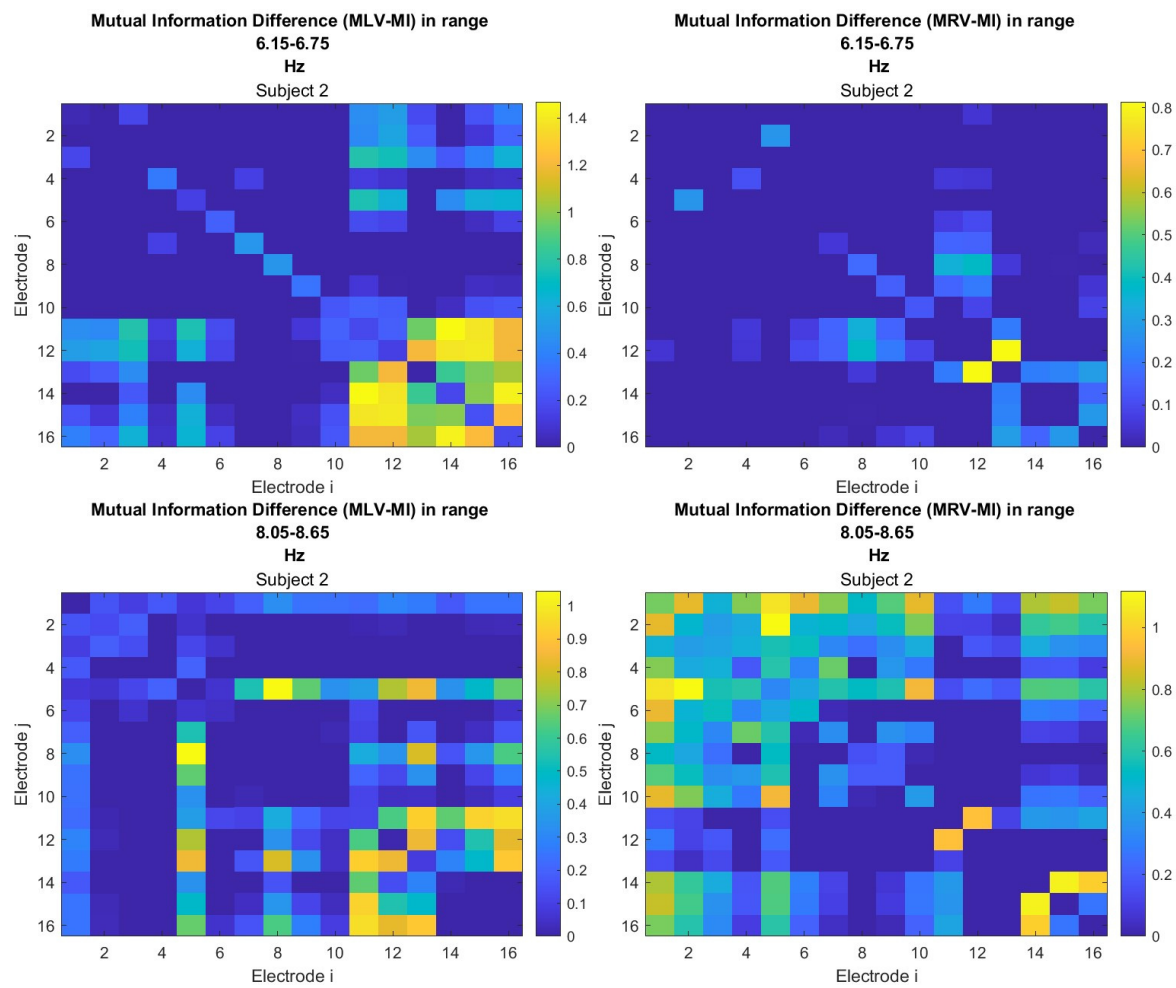


**Figure A5.** Increasing mutual information ( $\Delta Inf > 0$ ) associated with figurative attention to (left panels) left cube orientation and (right panels) at frequencies (upper row)  $f_1$  and (lower row)  $f_2$ .

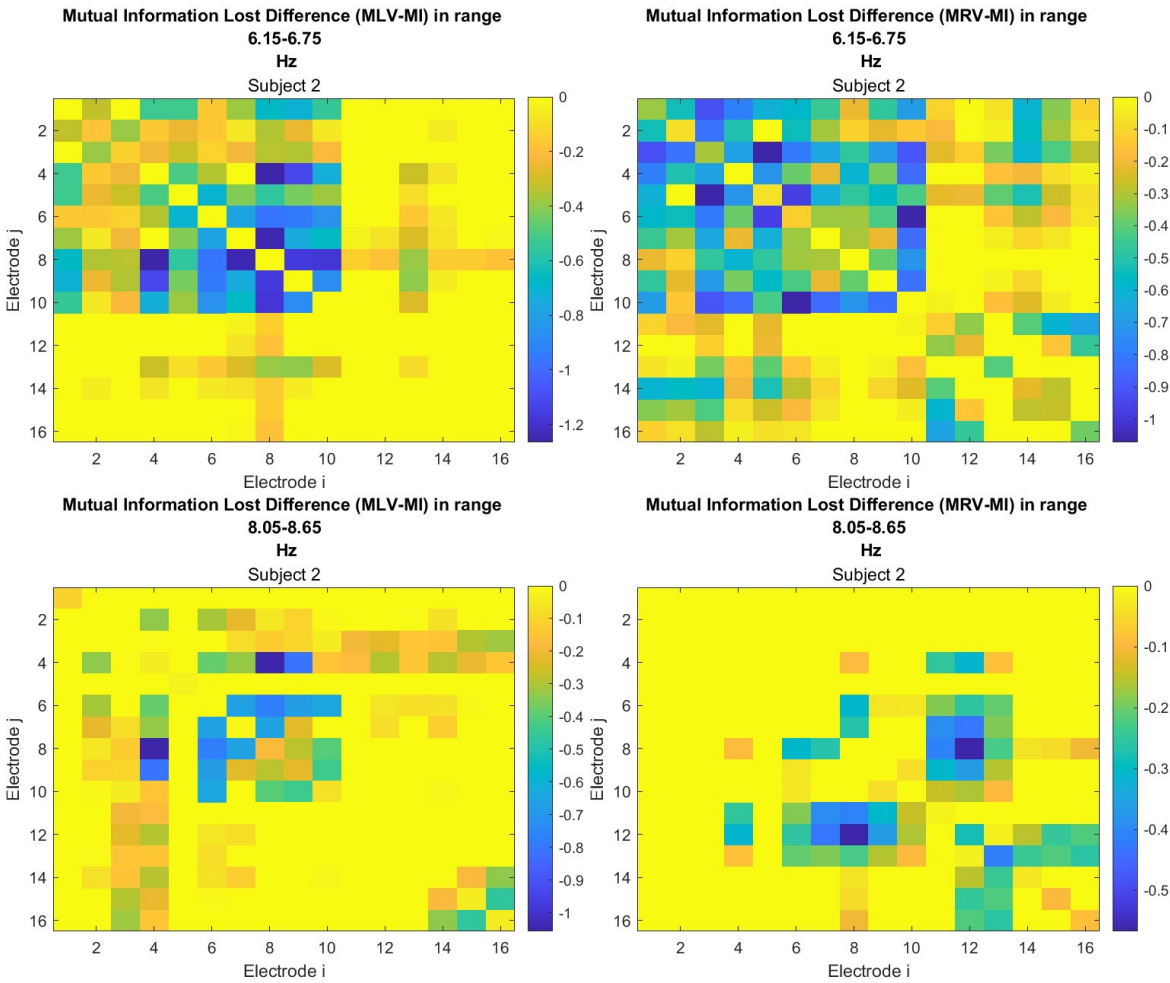


**Figure A6.** Decreasing mutual information ( $\Delta Inf < 0$ ) associated with figurative attention to (left panels) left cube orientation and (right panels) at frequencies (upper row)  $f_1$  and (lower row)  $f_2$ .

**Appendix B. Probability Measures**

The linear probability plots for explored connectivity measures are presented in Figures A7–A9.

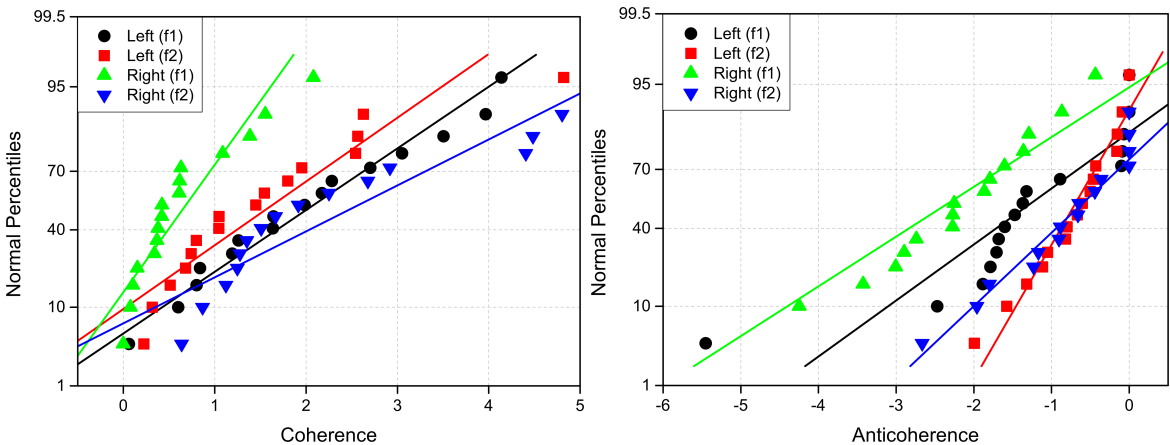


**Figure A7.** Normal probability plots of (left) coherence (Lab  $Coh_n > 0$ ) and (right) anticoherence (Lab  $Coh_n < 0$ ) labels. The reference lines have the same colors as percentiles.

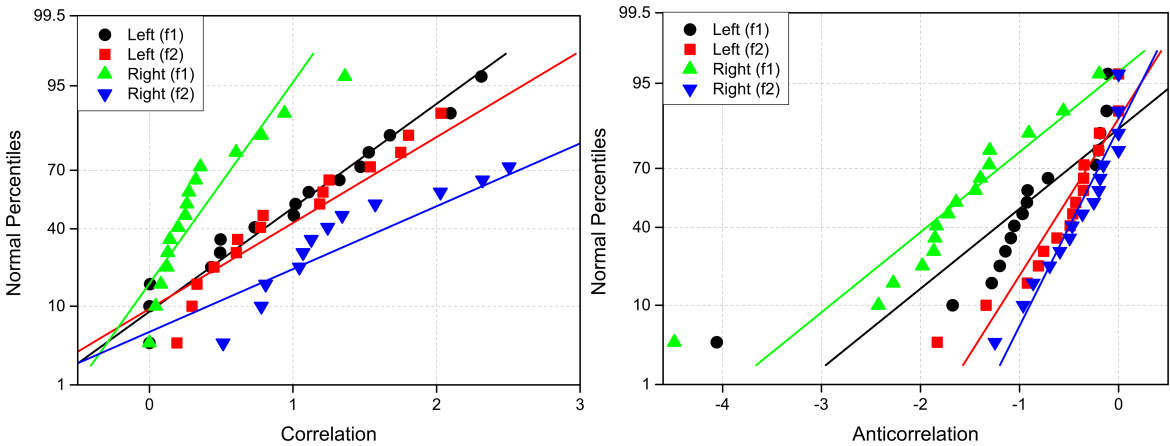


**Figure A8.** Normal probability plots of (left) correlation (Lab  $Corr_n > 0$ ) and (right) anticorrelation (Lab  $Corr < 0$ ) labels. The reference lines have the same colors as percentiles.

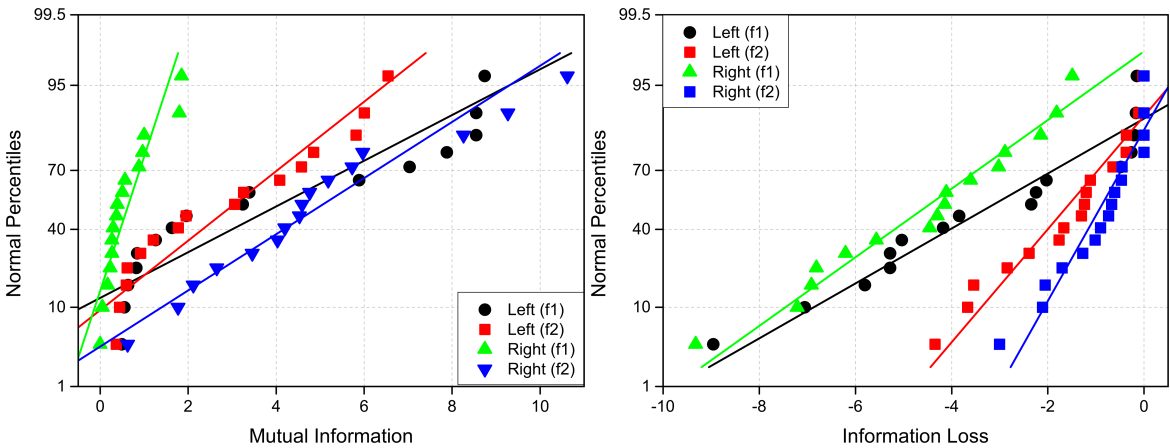


**Figure A9.** Normal probability plots of (left) mutual information (Lab  $Inf_n > 0$ ) and (right) information loss (Lab  $Inf_n < 0$ ) labels. The reference lines have the same colors as percentiles.

Table A1 presents the means and standard deviations derived from the normal probability plots.

**Table A1.** Mean ( $M$ ), standard deviation ( $\sigma$ ), and threshold ( $C_{th}$ ) values for the following connectivity measures (**M**): coherence (Coh), anticorrelation (ACoh), correlation (Corr), anticorrelation (ACorr), mutual information (MInf), and information loss (ILoss).

M	Left $f_1$			Left $f_2$			Right $f_1$			Right $f_2$		
	$M$	$\sigma$	$C_{th}$	$m$	$\sigma$	$C_{th}$	$M$	$\sigma$	$C_{th}$	$M$	$\sigma$	$C_{th}$
Coh	1.99	1.18	3.17	1.54	1.14	2.69	0.64	0.57	1.21	2.45	1.59	4.04
ACoh	-1.37	1.31	-2.68	-0.73	0.55	-1.28	-2.45	1.48	-3.92	-0.73	0.55	-1.28
Corr	0.98	0.70	1.68	1.15	0.85	2.00	0.37	0.36	0.73	1.95	1.16	3.11
ACorr	-0.99	0.92	-1.91	-0.57	0.47	-1.04	-1.70	0.91	-2.62	-0.40	0.37	-0.78
MInf	3.84	3.21	7.05	2.88	2.11	4.99	0.60	0.55	1.15	4.86	2.62	7.48
ILoss	-3.33	2.67	-6.01	-1.66	1.30	-2.96	-4.63	2.14	-6.77	-0.94	0.86	-1.80

References

1. Towle, V.L.; Hunter, J.D.; Edgar, J.C.; Chkhenkeli, S.A.; Castelle, M.C.; Frim, D.M.; Kohrman, M.; Hecox, K. Frequency domain analysis of human subdural recordings. *J. Clin. Neurophysiol.* **2007**, *24*, 205–213.

2. Hramov, A.E.; Frolov, N.S.; Maksimenko, V.A.; Kurkin, S.A.; Kazantsev, V.B.; Pisarchik, A.N. Functional networks of the brain: from connectivity restoration to dynamic integration. *Phys. Uspekhi* **2021**, *64*, 584–616.

3. Boccaletti, S.; De Lellis, P.; del Genio, C.; Alfaro-Bittner, K.; Criado, R.; Jalan, S.; Romance, M. The structure and dynamics of networks with higher order interactions. *Phys. Rep.* **2023**, *1018*, 1–64.
4. Bullmore, E.; Sporns, O. Complex brain networks: graph theoretical analysis of structural and functional systems. *Nat. Rev. Neurosci.* **2009**, *10*, 186–198.
5. Friston, K.J. Functional and effective connectivity: a review. *Brain Connectivity* **2011**, *1*, 13–36.
6. Tavor, I.; Jones, O.P.; Mars, R.; Smith, S.; Behrens, T.; Jbabdi, S. Task-free MRI predicts individual differences in brain activity during task performance. *Science* **2016**, *352*, 216–220.
7. Greicius, M. Resting-state functional connectivity in neuropsychiatric disorders. *Curr. Opin. Neurol.* **2008**, *21*, 424–430.
8. Zhang D, R.M. Disease and the brain's dark energy. *Nat. Rev. Neurol.* **2010**, *6*, 15–28.
9. Dennis, E.L.; Thompson, P.M. Functional brain connectivity using fMRI in aging and Alzheimer's disease. *Neuropsychol. Rev.* **2014**, *24*, 49–62.
10. Tomasi, D.; Volkow, N.D. Aging and functional brain networks. *Mol. Psychiatry* **2012**, *17*, 549–558.
11. Sala-Llonch, R.; Bartrés-Faz, D.; Junqué, C. Reorganization of brain networks in aging: a review of functional connectivity studies. *Front. Psychol.* **2015**, *6*.
12. Contreras, J.A.; Goñi, J.; Risacher, S.L.; Sporns, O.; Saykin, A.J. The structural and functional connectome and prediction of risk for cognitive impairment in older adults. *Curr. Behav. Neurosci. Rep.* **2015**, *2*, 234–245.
13. Davison, E.N.; Turner, B.O.; Schlesinger, K.J.; Miller, M.B.; Grafton, S.T.; Bassett, D.S.; Carlson, J.M. Individual differences in dynamic functional brain connectivity across the human lifespan. *PLoS Comput. Biol.* **2016**, *12*, e1005178.
14. Zuo, X.N.; Ehmke, R.; Mennes, M.; Imperati, B.; Castellanos, F.X.; Sporns, O.; et al.. Network centrality in the human functional connectome. *Cerebral Cortex* **2012**, *22*, 1862–1875.
15. Greene, A.S.; Gao, S.; Scheinost, D.; Constable, R.T. Task-induced brain state manipulation improves prediction of individual traits. *Nat. Commun.* **2018**, *9*, 2807.
16. Gu, S.; Yang, M.; Medaglia, J.D.; Gur, R.C.; Gur, R.E.; Satterthwaite, T.D.; Bassett, D.S. Functional hypergraph uncovers novel covariant structures over neurodevelopment. *Human Brain Mapping* **2017**, *38*, 3823–3835.
17. Xiao, L.; Wang, J.; Kassani, P.H.; Zhang, Y.; Bai, Y.; Stephen, J.M.; Wilson, T.W.; Calhoun, V.D.; Wang, Y.P. Multi-hypergraph learning based brain functional connectivity analysis in fMRI data. *IEEE Trans. Medical Imaging* **2020**, *39*, 1746–1758.
18. Ji, Y.; Zhang, Y.; Shi, H.; Jiao, Z.; Wang, S.H.; Wang, C. Constructing dynamic brain functional networks via hyper-graph manifold regularization for mild cognitive impairment classification. *Front. Neurosci.* **2021**, *15*, 669345.
19. Ji, J.; Ren, Y.; Lei, M. FC-HAT: Hypergraph attention network for functional brain network classification. *Information Sciences* **2022**, *608*, 1301–1316.
20. Wu, K.; Song, X.; Chai, L. Graph metrics based brain hypergraph learning in schizophrenia patients. In Proceedings of the Proceedings of the 2022 China Automation Congress (CAC), Xiamen, China, November 2022; pp. 3251–3256.
21. Xi, Z.; Liu, T.; Shi, H.; Jiao, Z. Hypergraph representation of multimodal brain networks for patients with end-stage renal disease associated with mild cognitive impairment. *Math. Biosci. Eng.* **2023**, *20*, 1882–1902.
22. Wang, J.; Li, H.; Qu, G.; Cecil, K.M.; Dillman, J.R.; Parikh, N.A.; He, L. Dynamic weighted hypergraph convolutional network for brain functional connectome analysis. *Medical Image Analysis* **2023**, *87*, 102828.
23. Niua, J.; Dua, Y. Applications of hypergraph-based methods in classifying and subtyping psychiatric disorders: a survey. *Radiology Science* **2023**, *2*, 83–95.
24. Yang, J.; Hu, M.; Hu, Y.; Zhang, Z.; Zhong, J. Diagnosis of autism spectrum disorder (ASD) using recursive feature elimination-graph neural network (RFE-GNN) and phenotypic feature extractor (PFE). *Sensors* **2023**, *23*, 9647.
25. Hao, X.; Li, J.; Ma, M.; Qin, J.; Zhang, D.; Liu, F.; for Alzheimer's Disease Neuroimaging Initiative. Hypergraph convolutional network for longitudinal data analysis in Alzheimer's disease. *Computers in Biology and Medicine* **2024**, *168*, 107765.
26. Gao, X.; Zhu, Y.; Yang, Y.; Zhang, F.; Zhou, F.; Tian, X.; Xu, K.; Chen, Y. A seizure detection method based on hypergraph features and machine learning. *Biomedical Signal Processing and Control* **2022**, *77*, 103769.
27. Li, M.; Qiu, M.; Zhu, L.; Kong, W. Feature hypergraph representation learning on spatial-temporal correlations for EEG emotion recognition. *Cognitive Neurodynamics* **2023**, *17*, 1271–1281.



28. Zhu, L.; Liu, Y.; Liu, R.; Peng, Y.; Cao, J.; Li, J.; Kong, W. Decoding multi-brain motor imagery from EEG using coupling feature extraction and few-shot learning. *IEEE Trans. Neural Syst. Rehabil. Eng.* **2023**, *31*, 4683–4692.
29. Liu, M.; Zhang, J.; Yap, P.T.; Shen, D. View-aligned hypergraph learning for Alzheimer's disease diagnosis with incomplete multi-modality data. *Medical Image Analysis* **2017**, *36*, 123–134.
30. Peña Serrano, N.; Jaimes-Reátegui, R.; Pisarchik, A.N. Hypergraph of functional connectivity based on event-related coherence: Magnetoencephalography data analysis. *Appl. Sci.* **2024**, *14*, 2343.
31. Bretto, A. *Hypergraph Theory: An Introduction*; Mathematical Engineering, Springer: Cham, 2013.
32. Dai, Q.; Gao, Y. *Hypergraph Computation*; Springer: Singapore, 2023.
33. Xi, Z.; Liu, T.; Shi, H.; Jiao, Z. Hypergraph representation of multimodal brain networks for patients with end-stage renal disease associated with mild cognitive impairment. *Math. Biosci. Eng.* **2022**, *20*, 1882–1902.
34. Wang, Z.; Liu, J.; Zhong, N.; Qin, Y.; Zhou, H.; Yang, J.; Li, K., A naïve hypergraph model of brain networks. In *Brain Informatics. BI 2012. Lecture Notes in Computer Science*; Zanzotto, F.M.; Tsumoto, S.; Taatgen, N.; Yao, Y., Eds.; Springer-Verlag: Berlin, Heidelberg, 2012; Vol. 7670, pp. 119–129.
35. Caetano e Souza, R.H.; Martins Naves, E.L. Attention detection in virtual environments using EEG signals: A Scoping review. *Front. Physiol.* **2021**, *12*, 727840.
36. Esqueda-Elizondo, J.J.; Juárez-Ramírez, R.; López-Bonilla, O.R.; García-Guerrero, E.E.; Galindo-Aldana, G.M.; Jiménez-Beristáin, L.; Serrano-Trujillo, A.; Tlelo-Cuautle, E.; Inzunza-González, E. Attention measurement of an autism spectrum disorder user using EEG signals: A case study. *Math. Comput. Appl.* **2022**, *27*, 21.
37. Mateos, D.M.; Krumm, G.; Arán Filippetti, V.; Gutierrez, M. Power spectrum and connectivity analysis in EEG recording during attention and creativity performance in children. *NeuroSci.* **2022**, *3*, 347–365.
38. Al-Naffan, A.; Aldayel, M. Predict students' attention in online learning using EEG data. *Sustainability* **2022**, *14*, 6553.
39. Escalante Puente de la Vega, W.; Imbert Paredes, R.; Villalba Mora, E.; Pisarchik, A.N. Figurative attention: EEG-based assessment using ambiguous stimuli. *Preprint (Research Square)* **2025**. <https://doi.org/10.21203/rs.3.rs-4590719/v1>.
40. Bowyer, S.M. Coherence a measure of the brain networks: past and present. *Neuropsychiatr. Electrophysiol.* **2016**, *2*, 1–12.
41. Chiarion, G.; Sparacino, L.; Antonacci, Y.; Faes, L.; Mesin, L. Connectivity analysis in EEG data: A tutorial review of the state of the art and emerging trends. *Bioeng.* **2023**, *10*, 372.
42. Jeong, J.; Gore, J.C.; Peterson, B.S. Mutual information analysis of the EEG in patients with Alzheimer's disease. *Clinical Neurophysiology* **2001**, *112*, 827–835. [https://doi.org/https://doi.org/10.1016/S1388-2457\(01\)00513-2](https://doi.org/https://doi.org/10.1016/S1388-2457(01)00513-2).
43. Chholak, P.; Maksimenko, V.A.; Hramov, A.E.; Pisarchik, A.N. Voluntary and involuntary attention in bistable visual perception: A MEG study. *Front. Hum. Neurosci.* **2020**, *14*, 597895. <https://doi.org/10.3389/fnhum.2020.597895>.
44. Liu, Y.; Safavi, T.; Dighe, A.; Koutra, D. Graph summarization methods and applications: A survey. *ACM Computing Surveys* **2018**, *51*, 62.
45. Maccioni, A.; Abadi, D.J. Scalable pattern matching over compressed graphs via dedensification. In *Proceedings of the Proceedings of the ACM Conference on Knowledge Discovery and Data Mining (KDD'16)*. ACM Press, 2016, pp. 1755–1764.
46. Andrew, C.; Pfurtscheller, G. Event-related coherence as a tool for studying dynamic interaction of brain regions. *Electroencephalogr. Clin. Neurophysiol.* **1996**, *98*, 144–148.
47. Pisarchik, A.; Hramov, A. Coherence resonance in neural networks: Theory and experiments. *Phys. Rep.* **2023**, *1000*, 1–57.
48. Gross, J.; Schmitz, F.; Schnitzler, I.; Kessler, K.; Shapiro, K.; Hommel, B.; Schnitzler, A. Modulation of long-range neural synchrony reflects temporal limitations of visual attention in humans. *Proc. Natl. Acad. Sci. USA* **2004**, *101*, 13050–13055.
49. Guggisberg, A.G.; Honma, S.M.; Findlay, A.M.; Dalal, S.S.; Kirsch, H.E.; Berger, M.S.; Nagarajan, S.S. Mapping functional connectivity in patients with brain lesions. *Ann. Neurol.* **2008**, *63*, 193–203.
50. Belardinelli, P.; Ciancetta, L.; Staudt, M.; Pizzella, V.; Londei, A.; Birbaumer, N.; Romani, G.L.; Braun, C. Cerebro-muscular and cerebro-cerebral coherence in patients with pre- and perinatally acquired unilateral brain lesions. *NeuroImage* **2007**, *37*, 1301–1314.

51. de Pasquale, F.; Della Penna, S.; Snyder, A.Z.; Lewis, C.; Mantini, D.; Marzetti, L.; Belardinelli, P.; Ciancetta, L.; Pizzella, V.; Romani, G.L.; et al. Temporal dynamics of spontaneous MEG activity in brain networks. *Proc. Natl. Acad. Sci. USA* **2010**, *107*, 6040–6045.
52. Kim, J.S.; Shin, K.S.; Jung, W.H.; Kim, S.N.; Kwon, J.S.; Chung, C.K. Power spectral aspects of the default mode network in schizophrenia: an MEG study. *BMC Neurosci.* **2014**, *15*, 104.
53. Bowyer, S.M.; Gjini, K.; Zhu, X.; Kim, L.; Moran, J.E.; Rizvi, S.U.; Gumenyuk, N.T.; Tepley, N.; Boutros, N.N. Potential biomarkers of schizophrenia from MEG resting-state functional connectivity networks: Preliminary data. *J. Behav. Brain Sci.* **2015**, *5*, 1.
54. Boutros, N.N.; Galloway, M.P.; Ghosh, S.; Gjini, K.; Bowyer, S.M. Abnormal coherence imaging in panic disorder: a magnetoencephalography investigation. *Neuroreport* **2013**, *24*, 487–491.
55. Chholak, P.; Niso, G.; Maksimenko, V.A.; Kurkin, S.A.; Frolov, N.S.; Pitsik, E.N.; Hramov, A.E.; Pisarchik, A.N. Visual and kinesthetic modes affect motor imagery classification in untrained subjects. *Sci. Rep.* **2019**, *9*, 1–12.
56. Pisarchik, A.N.; Chholak, P.; Hramov, A.E. Brain noise estimation from MEG response to flickering visual stimulation. *Chaos Solitons Fractals X* **2019**, *1*, 100005.
57. Baldassarre, A.; Lewis, C.M.; Committeri, G.; Snyder, A.Z.; Luca Romani, G.; Corbetta, M. Individual variability in functional connectivity predicts performance of a perceptual task. *Proc. Natl. Acad. Sci.* **2012**, *109*, 3516–3521.
58. Kashyap, R.; Kong, R.; Bhattacharjee, S.; Li, J.; Zhou, J.; Thomas Yeo, B.T. Individual-specific fMRI-Subspaces improve functional connectivity prediction of behavior. *NeuroImage* **2019**, *189*, 804–812.
59. Shannon, C.E.; Weaver, W. *The mathematical theory of communication*; University of Illinois Press: Urbana, 1949.
60. Cover, T.M.; Thomas, J.A. *Elements of information theory*; John Wiley & Sons: New York, 1991.
61. GitLab.com, howpublished = [https://gitlab.com/bci\\_project/visual\\_stimulation\\_codes/datas\\_eeg](https://gitlab.com/bci_project/visual_stimulation_codes/datas_eeg), note = Accessed: 2025-10-02.
62. Isoglu-Alkaç, U.; Basar-Eroglu, C.; Ademoglu, A.; Demiralp, T.; Miener, M.; Stadler, M. Alpha activity decreases during the perception of necker cube reversals: An application of wavelet transform. *Biol Cybern* **2000**, *82*, 313–320.
63. Adeli, H.; Zhou, Z.; Dadmehr, N. Analysis of EEG records in an epileptic patient using wavelet transform. *J. Neurosci. Methods* **2003**, *123*, 69–87.
64. Ghuman, A.S.; McDaniel, J.R.; Martin, A. A wavelet-based method for measuring the oscillatory dynamics of resting-state functional connectivity in MEG. *Neuroimage* **2011**, *56*, 69–77.
65. Maksimenko, V.A.; Hramov, A.E.; Grubov, V.V.; Nedaivozov, V.O.; Makarov, V.V.; Pisarchik, A.N. Nonlinear effect of biological feedback on brain attentional state. *Nonlin. Dyn.* **2019**, *95*, 1923–1939.
66. Maksimenko, V.A.; Frolov, N.S.; Hramov, A.E.; Runnova, A.E.; Grubov, V.V.; Kurths, J.; Pisarchik, A.N. Neural interactions in a spatially-distributed cortical network during attentional tasks. *Front. Behav. Neurosci.* **2019**, *13*, 220.
67. Khramova, M.V.; Kuc, A.K.; Maksimenko, V.A.; Frolov, N.S.; Grubov, V.V.; Kurkin, S.A.; Pisarchik, A.N.; Shusharina, N.N.; Fedorov, A.A.; Hramov, A.E. Monitoring the cortical activity of children and adults during cognitive task completion. *Sensors* **2021**, *21*, 6021.
68. Fang, Q.; Sang, J.; Xu, C.; Rui, Y. Topic-sensitive influencer mining in interest-based social media networks via hypergraph learning. *IEEE Trans Multimed* **2014**, *16*, 796–812.
69. Martinet, L.E.; Kramer, M.; Viles, W.; Perkins, L.; Spencer, E.; et al.. Robust dynamic community detection with applications to human brain functional networks. *Nat Commun* **2020**, *11*, 2785.
70. Zhao, Z.; Yang, K.; Guo, J. Link prediction with hypergraphs via network embedding. *Appl. Sci.* **2023**, *13*, 523.
71. Berge, C. *Graphs and Hypergraphs*; North-Holland: Amsterdam, 1976.
72. Bi, X.A.; Wang, Y.; Luo, S.; Chen, K.; Xing, Z.; Xu, L. Hypergraph structural information aggregation generative adversarial networks for diagnosis and pathogenetic factors identification of Alzheimer's disease with imaging genetic data. *IEEE Trans. Neural Netw. Learn. Syst.* **2024**, *35*, 7420–7434.

**Disclaimer/Publisher's Note:** The statements, opinions and data contained in all publications are solely those of the individual author(s) and contributor(s) and not of MDPI and/or the editor(s). MDPI and/or the editor(s) disclaim responsibility for any injury to people or property resulting from any ideas, methods, instructions or products referred to in the content.